NASA Contractor Report 3075

A Computational Model for the Prediction of Jet Entrainment in the Vicinity of Nozzle Boattails (The BOAT Code)

Sanford M. Dash and Harold S. Pergament

CONTRACT NAS1-14794
DECEMBER 1978

NASA

NASA Contractor Report 3075

A Computational Model for the Prediction of Jet Entrainment in the Vicinity of Nozzle Boattails (The BOAT Code)

Sanford M. Dash and Harold S. Pergament
Aeronautical Research Associates of Princeton, Inc.
Princeton, New Jersey

Prepared for
Langley Research Center
under Contract NAS1-14794

National Aeronautics
and Space Administration

Scientific and Technical
Information Office

1978

TABLE OF CONTENTS

LIST OF FIGURES

NOMENCLATURE

A	$\mu_t \rho u r^2/\psi$
$C_{D,\beta}$	afterbody (pressure) drag coefficient
C_p	afterbody pressure coefficient, $C_p = (p - p_e)/\frac{1}{2}\rho_e u_e^2$
c_p	specific heat
D	maximum afterbody diameter
F_i	X_i/W
h_i	enthalpy of i^{th} species
k	turbulent kinetic energy
ℓ	length scale for Prandtl mixing length model
M	Mach number
p	pressure
Px	pressure gradient in x direction
Pr	turbulent Prandtl number
r	radial distance from axis
r_{eff}	radial distance to effective inviscid boundary
r_j	nozzle exit radius
T	static temperature
u^*	frictional velocity, $u^* = \tau_w/\rho u^2$
u, U	axial velocity
$\overline{uv}$	proportional to turbulent shear stress
v	radial velocity
v_j	injection velocity
W	mixture molecular weight
$w(\xi)$	Cole's universal wake function, Eq. (15)
Le	turbulent Lewis number
$\dot{w}_i$	net rate of production of the i^{th} species

x	axial distance
x_c	core length
X_i	mole fraction of i^{th} species
y	distance normal to inviscid plume interface
$y_{1/2}$	normal distance to point where $u = \frac{1}{2}(u_2 + u_1)$
γ	ratio of specific heats
δ	boundary layer thickness; also characteristic mixing layer thickness
δ^*	boundary layer displacement thickness
ε	turbulent dissipation rate
μ_t	turbulent viscosity
ρ	density
σ	shear layer spreading parameter, defined by Eq. (44)
σ_o	spreading parameter for $u_2/u_1 = 0$
σ_k	Prandtl number for turbulent kinetic energy
σ_ε	Prandtl number for turbulent dissipation
τ_w	wall shear stress
ψ	stream function

Subscripts

c	centerline
e,E	external flow
j,J	exhaust plume (jet) flow
1	inner mixing layer boundary
2	outer mixing layer boundary
t	stagnation
I	inner stream
i	refers to i^{th} species

1. SUMMARY

The development of a computational model (BOAT) for calculating nearfield jet entrainment, and its incorporation in an existing methodology for the prediction of nozzle boattail pressures, is discussed. BOAT accounts for the detailed turbulence and thermochemical processes occurring in the mixing layer formed between a jet exhaust and surrounding external stream while interfacing with the inviscid exhaust and external flowfield regions in an overlaid, interactive manner. The ability of the BOAT model to analyze simple free shear flows is assessed by detailed comparisons with fundamental laboratory data. The overlaid procedure for incorporating variable pressures into BOAT and the entrainment correction employed to yield an "effective" plume boundary for the inviscid external flow are demonstrated. This is accomplished via application of BOAT in conjunction with the codes comprising the NASA/LRC patched viscous/inviscid methodology for determining nozzle boattail drag for subsonic/transonic external flows. An assessment of the overall approach is provided via comparisons between these predictions and data for underexpanded laboratory cold air jets. A manual describing the operation of the BOAT code comprises a supplement to this report.

2. INTRODUCTION

The accurate prediction of nozzle boattail drag requires a detailed description of the coupled viscous/inviscid flow processes occurring along the nozzle afterbody and in the nearfield mixing layer growing along the plume interface which separates the nozzle exhaust and external air streams (Fig. 2.1). While analyses based upon solving the turbulent Navier-Stokes equations can provide a description of this complex flowfield, the widely disparate length scales and flow characteristics in the various regions involved lead to rather prohibitive computer time requirements in achieving results of adequate resolution. A more efficient procedure is that provided by a "patched" viscous/inviscid methodology where each region is separately analyzed by computational procedures specifically catered to the flow processes and length scales occurring within that region. The overall flowfield solution is arrived at by patching these regional solutions together in an iterative manner. Such a patched methodology has been implemented at NASA/LRC[1,2,3] for subsonic/transonic external flows. For nonseparated afterbody flows, the LRC system presently includes the relaxation procedure of South and Jameson[4] for analyzing the inviscid subsonic/transonic external flow, the supersonic exhaust plume model of Salas[5], and an extended version of the Reshotko-Tucker[6] turbulent boundary layer integral method.

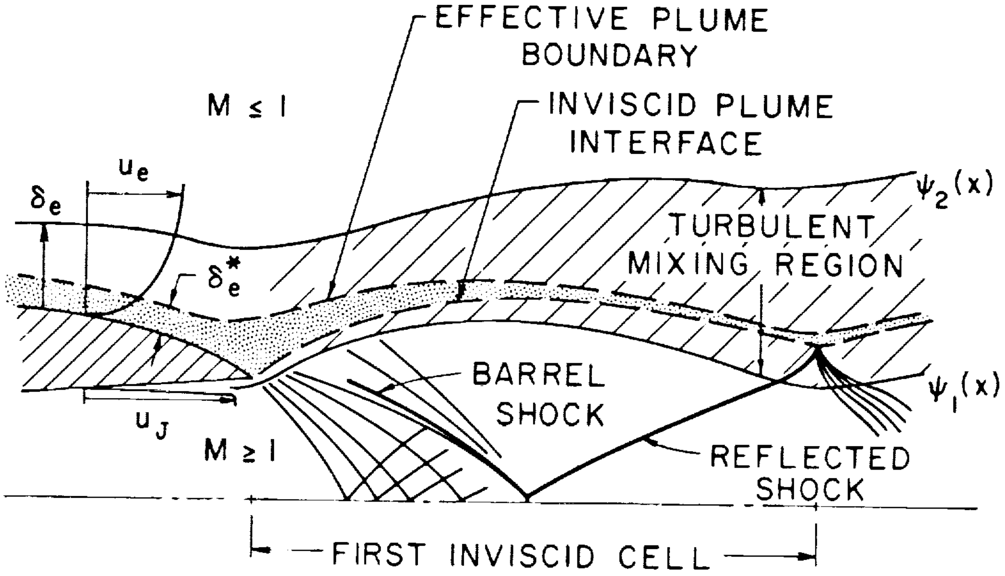

Figure 2.1 Schematic of afterbody/jet exhaust flowfield.

In past applications of the patched LRC system to afterbody/exhaust flow configurations[2], the inviscid plume interface was treated as a solid surface in determining afterbody pressure distributions. This assumption yielded results which substantially underpredicted the afterbody drag, since the additional contribution of jet entrainment due to mixing processes along the interface was not included. The physical influence of jet entrainment is manifested in an overall reduction of the blockage effect of the inviscid plume. The incorporation of entrainment effects into the LRC system by a displacement thickness type correction to the inviscid plume boundary will be shown in this report to yield substantially improved drag predictions.

The BOAT code, developed to calculate these entrainment effects, solves the axisymmetric jet mixing equations for a reacting gas mixture by a mixed implicit/explicit finite-difference procedure in transformed (x,ψ) coordinates. In developing BOAT, the "best" features of several current mixing/afterburning models were combined to achieve rather unique computational capabilities. In this respect, BOAT employs: (1) the same generalized treatment of thermochemical processes and implicit/explicit streamline integration procedure used in the Low Altitude Plume Program (LAPP)[7] (the current JANNAF standardized model for analyzing mixing/afterburning processes in low altitude rocket exhaust plumes); (2) the same type of shear layer discretization, grid distribution, and growth rules used in the GENMIX code[8]; and (3) the same type of overlaid procedure for describing variable edge conditions and both normal and streamwise pressure gradients as used in the GASL "patched" system[9] for the detailed analysis of inviscid/shock and mixing/afterburning processes in rocket exhaust plumes. Previous entrainment models[10,11] have not accounted for pressure gradients and thermochemical effects. The present work will show that the neglect of pressure gradients can cause serious errors in the prediction of nearfield entrainment. While no detailed calculations have as yet been made for hot, afterburning plumes, it is apparent that real gas behavior and chemistry will affect nearfield entrainment.

Of critical importance in the overall modeling of nearfield jet entrainment is the selection of an appropriate turbulence model. Several turbulence models of varying complexity are presently incorporated in BOAT. For the low speed, nonreactive cases thus far considered, an extended version of the Prandtl mixing length (ML) model and/or $k\varepsilon 2$ two-equation turbulence model appear to yield results of sufficient quality. A description of these models and their assessment via comparisons with pertinent free shear layer experimental data will be discussed.

Applications of BOAT to the analysis of laboratory cold air jets have been performed and sensitivities to various parameters explored. Detailed experimental measurements in the underexpanded jet nearfield region are not presently available to adequately assess the individual modeling procedures employed. The validity of the overall approach must therefore be established by comparisons between predicted boattail pressure distributions (via application of BOAT in conjunction with the other components of the patched LRC system) and measured boattail pressures for the cold air jets[12]. These comparisons are presented herein and the sensitivity of predicted boattail pressures to various model parameters is discussed in some detail.

The overall methodology is discussed in Section 3, while the computational procedures incorporated in the BOAT code are detailed in Section 4 of this report. Section 5 describes the validation of the code via comparisons with data used in the 1972 NASA Langley Free Turbulent Shear Flows Conference[13]. Section 6 describes its application to laboratory cold air jets, which simulate conditions for actual aircraft nozzles. The supplement to this report contains a detailed description of the operational procedures employed within BOAT, including a complete listing and comprehensive users manual. The displacement thickness-type correction introduced in this study and the methodology for incorporating BOAT in the overall patched system were jointly formulated by the authors and Dr. R.G. Wilmoth of LRC, who additionally performed the systematic calculations for the cold air jet cases reported in Section 6.

3. METHODOLOGY

3.1 Background

In developing the BOAT code, a review of several widely used, well tested models was undertaken with the objective of assessing their best features and incorporating these features into BOAT. The models reviewed included the LAPP code[7], the GENMIX code[8], and the GASL plume model[9].

The popularity of the LAPP code[7] is largely attributable to its ease of usage and overall reliability. LAPP calculates the constant pressure mixing between concentric, chemically reacting streams. The governing parabolic mixing layer equations are solved in Von Mises (x,ψ) coordinates using a mixed implicit/explicit computational procedure. In particular, the species continuity equation is solved in a coupled fashion using an implicit, linearized procedure which permits substantially larger integration step sizes in chemical near-equilibrium situations than explicit procedures. The computational scheme requires the definition of grid points from the jet axis to the upper mixing layer boundary, thus precluding a refined definition of nearfield shear layers as well as the treatment of initial boundary layers. Mixing layer growth occurs via the addition of grid points at the upper boundary which is numerically cumbersome and can be rather inaccurate. Arbitrary chemical reaction mechanisms can be treated via the input of appropriate forward rate constants and thermodynamic data.

The BOAT code closely follows the overall methodology employed in LAPP. Since only the nearfield shape of the "effective" plume boundary (i.e., its shape in the first inviscid cell or wave length) significantly influences nozzle boattail pressures[2], the principal modifications in this methodology have been geared to improving the computational accuracy in the nearfield shear layer. A rather efficient approach for treating nearfield shear layers was introduced by Patankar and Spalding in the GENMIX code[8]. Here, the computational domain spans the shear layer which is solved in a mapped x,ω coordinate system*. The growth of the shear layer is determined by specified rules related to property variations at the edges. This approach has been adapted in BOAT.

The transformation to x,ω coordinates in GENMIX numerically confines the shear layer between $\omega = 0$ and 1, thus permitting its calculation to be performed with a fixed number of grid intervals. The equations in x,ω coordinates are lengthier than those in the x,ψ system and the integration process does not follow streamlines (i.e., lines of constant ω are not streamlines). The desirability of working in an x,ψ system is quite evident. However, previous models such as LAPP have not implemented this system in an effective manner in nearfield situations. Patankar and Spalding[8] discount the use of an x,ψ system entirely stating that "advantageous though (its use) may be in other respects, the grid nodes are still inefficiently distributed." In the BOAT code, however, a new computational procedure is employed which uses the x,ψ system for integrating the flowfield equations, yet efficiently distributes the grid nodes in a manner identical to the mapped x,ω system in GENMIX.

The requirement for employing a discretized shear layer approach in studies keyed to the accurate prediction of nearfield entrainment is quite evident from the results depicted in Figure 3.1. Here, BOAT with a fixed 11-point grid array is shown to predict the correct linear relation between mass entrainment and axial distance while LAPP, initialized with 21 points across the jet, requires more than two exit radii before the proper entrainment rate is asymptotically reached. In terms of profile shape, the LAPP prediction was poor at the two-radii location, showing a lack of convergence to the correct solution, while the BOAT calculation is in excellent agreement with experimental data, as will be detailed in Section 5.

---

*In GENMIX, the mapping is given by $\omega = [\psi - \psi_1(x)] / [\psi_2(x) - \psi_1(x)]$ where ψ_1 and ψ_2 are the streamfunction values at the upper (ψ_2) and lower (ψ_1) shear layer boundaries.

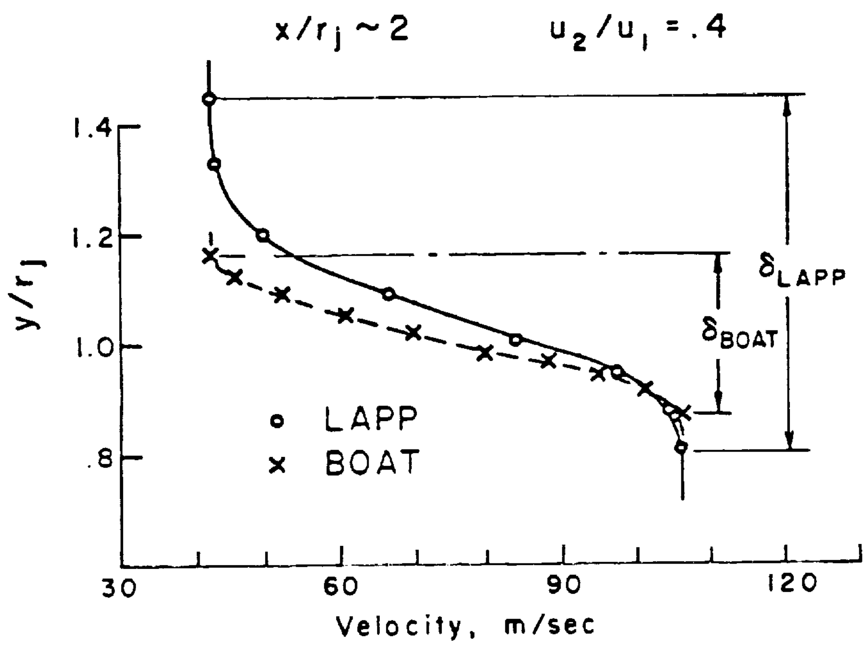

ENTRAINMENT COMPARISONS

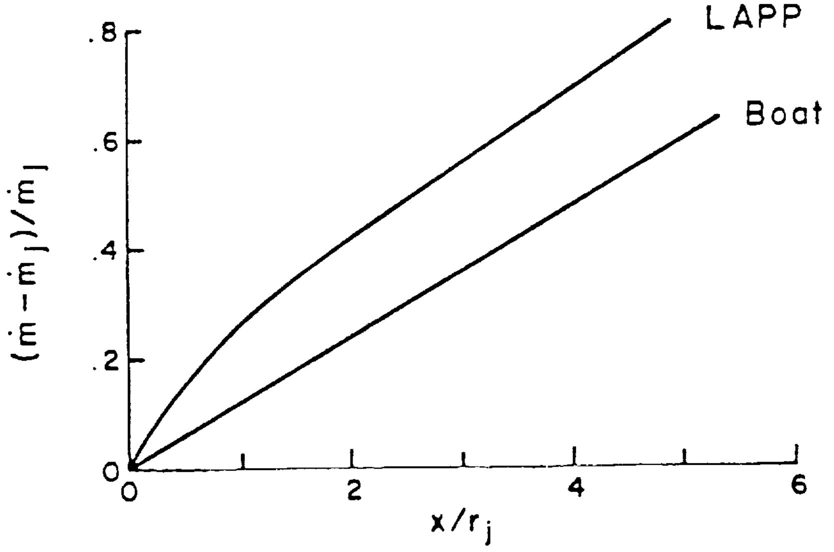

Figure 3.1 Comparison between LAPP and BOAT calculations in the nearfield shear layer. Both codes used Prandtl mixing length model.

For the incorporation of inviscid structure into the mixing/afterburning analysis, the "overlaid" approach introduced in the GASL plume model[9] has been adapted. The overlaid concept is a direct extension of classical boundary layer methodology to the analysis of nearfield shear layers. In boundary layer theory, the inviscid flow pattern is first calculated followed by a boundary layer calculation with edge conditions and pressure gradients set by the inviscid flow pattern. In the direct extension of this approach to nearfield shear layers, the inviscid exhaust plume and external flow patterns are first determined and the nearfield shear layer calculation is then initiated along the inviscid plume interface (see Fig. 3.2). Local edge conditions and both normal and streamwise pressure gradients are set in accordance with the calculated inviscid flow pattern and the rate of growth of the shear layer. The validity of this approach in application of the GASL model has been established by comparisons with various sets of experimental data. Selected comparisons are provided in the survey paper by Dash and Pergament[14].

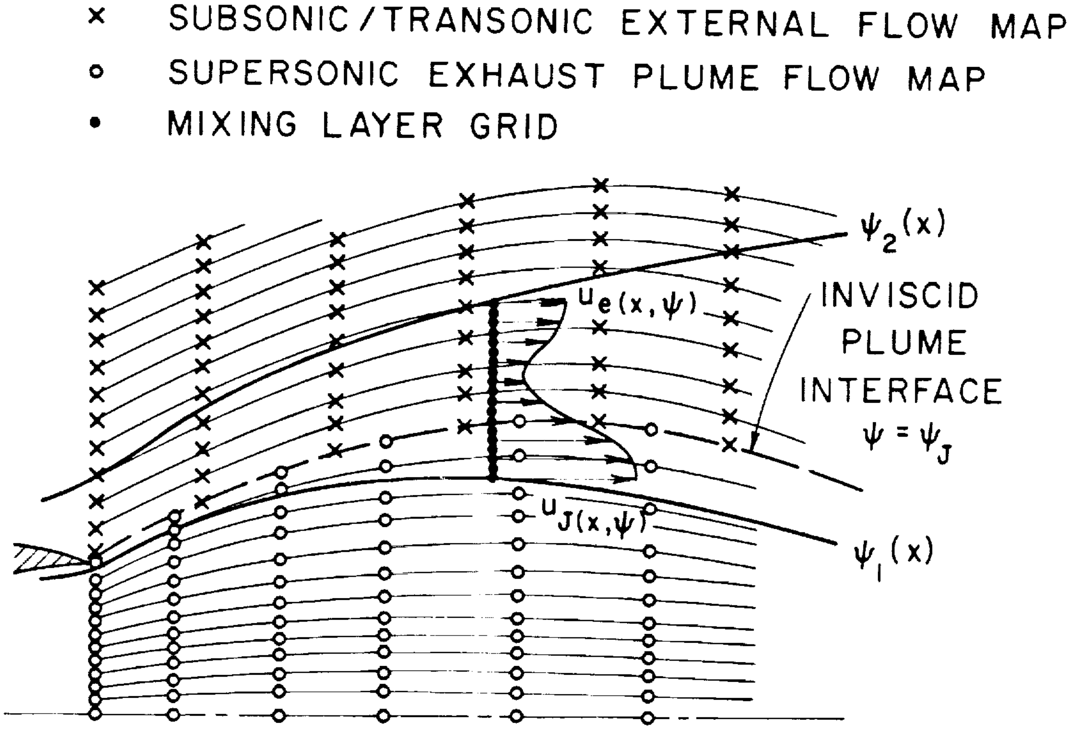

Figure 3.2 Schematic of mixing layer overlaid on jet exhaust and external flow maps.

3.2 Governing Equations

BOAT solves the parabolic jet mixing equations in transformed (x,ψ) coordinates. The resultant system of equations is listed below and includes equations for the turbulent kinetic energy, k, and dissipation, ε, as required in the two-equation turbulence model option.

Axial Momentum

$$\frac{\partial u}{\partial x} = -\frac{1}{\rho u}\frac{\partial p}{\partial x} + \frac{1}{\psi}\frac{\partial}{\partial \psi}\left(A\,\frac{\partial u}{\partial \psi}\right) \tag{1}$$

Energy

$$\begin{aligned} c_p\,\frac{\partial T}{\partial x} = {} & \frac{1}{\rho}\frac{\partial p}{\partial x} - \frac{1}{\rho u}\sum h_i \dot{w}_i + \frac{1}{\psi}\frac{\partial}{\partial \psi}\left(\frac{c_p}{Pr}\,A\,\frac{\partial T}{\partial \psi}\right) \\ & + \frac{A}{\psi}\left[\left(\frac{\partial u}{\partial \psi}\right)^2 + \frac{Le}{Pr}\frac{\partial T}{\partial \psi}\sum_i c_{p_i}\frac{\partial F_i}{\partial \psi}\right] \end{aligned} \tag{2}$$

Species Continuity

$$\frac{\partial F_i}{\partial x} = \frac{1}{\psi}\frac{\partial}{\partial \psi}\left(\frac{Le}{Pr}\,A\,\frac{\partial F_i}{\partial \psi}\right) + \frac{\dot{w}_i}{\rho u} \tag{3}$$

Turbulent Kinetic Energy

$$\frac{\partial k}{\partial x} = \frac{1}{\psi}\frac{\partial}{\partial \psi}\left(\frac{A}{\sigma_k}\frac{\partial k}{\partial \psi}\right) + \frac{1}{u}\,(P - \varepsilon) \tag{4}$$

Turbulent Dissipation

$$\frac{\partial \varepsilon}{\partial x} = \frac{1}{\psi}\frac{\partial}{\partial \psi}\left(\frac{A}{\sigma_\varepsilon}\frac{\partial \varepsilon}{\partial \psi}\right) + \frac{\varepsilon}{uk}\left(C_1 P - C_2 \varepsilon\right) \tag{5}$$

where

$$A = \mu_t\,\frac{\rho u r^2}{\psi}$$

$$P = \frac{Au}{\psi}\left(\frac{\partial u}{\partial \psi}\right)^2$$

and the transformation from (x,r) to (x,ψ) coordinates is given by

$$\begin{aligned} \psi\,\frac{\partial \psi}{\partial r} &= \rho u r \\ \psi\,\frac{\partial \psi}{\partial x} &= -\rho v r \end{aligned} \tag{6}$$

The above equations adequately describe mixing/afterburning processes in the nearfield shear layer for mildly underexpanded plumes, as well as in the farfield mixing layer. For plumes with significant underexpansion, nearfield mixing processes are more appropriately described in plume-oriented boundary layer coordinates measured along and normal to the inviscid plume interface. A discussion of the equations and methodology entailed in this system is provided in Reference 14.

3.3 Effective Plume Boundary Concept

The mechanism for modifying the inviscid plume geometry to account for entrainment is a direct extension of the weak interaction approach in standard boundary layer (BL) theory. In BL theory, the solid wall shape must be modified so that the "new" effective wall shape induces streamline deflections in the inviscid solution compatible with the viscous flow pattern. A standard modification involves applying an injection velocity boundary condition, $v(x)$, along the solid wall shape, or adding a displacement thickness, $\delta^*(x)$, to the solid wall shape (Fig. 3.3). For two-dimensional flows and axisymmetric flow situations where the BL thickness is small relative to the transverse body dimension, the normal velocity at the BL edge, $v_e(x)$, may simply be applied along the solid surface. For "thick" axisymmetric boundary layers, the $v(x)$ distribution applied along the surface must be modified from the edge distribution, $v_e(x)$, to satisfy the continuity equation. The displacement thickness variation, $\delta^*(x)$, is readily determined from the normal velocity distribution, $v(x)$, by solution of the differential equation

$$\frac{d\delta^*}{dx} = \frac{v}{u} \tag{7}$$

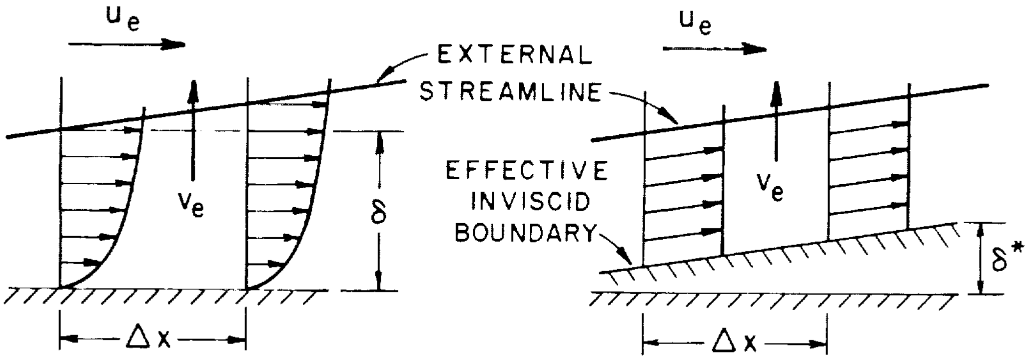

Figure 3.3 Effective boundary concept for a wall boundary layer.

In extending this concept to shear layers and the resulting modification of the inviscid plume geometry, we simply seek an appropriate boundary condition for the inviscid external flow calculation that will reproduce the normal velocity distribution, $v_e(x)$, at the outer edge of the shear layer (Fig. 3.4). If the entrainment induced flow deflections are small in comparison to the streamline deflections induced by the inviscid plume geometry (i.e., the "blockage effect"), the analogy with the BL problem is quite straightforward. Referring to Figure 3.5, the inviscid plume geometry can be properly modified by prescribing the inflow velocity, $v_e(x)$, along the inviscid plume interface in the repetition of the external flow calculation. Equivalently, the displacement thickness, $\delta^*(x)$, can be added to the inviscid interface yielding a new "effective" plume geometry. The specific choice between these two methods is somewhat arbitrary. The effective geometry concept provides a smoothing effect via the integration of the $v_e(x)$

distribution and was chosen for use in the subsequent calculation primarily because the external flow code[4] presently utilizes a geometric type boundary condition.

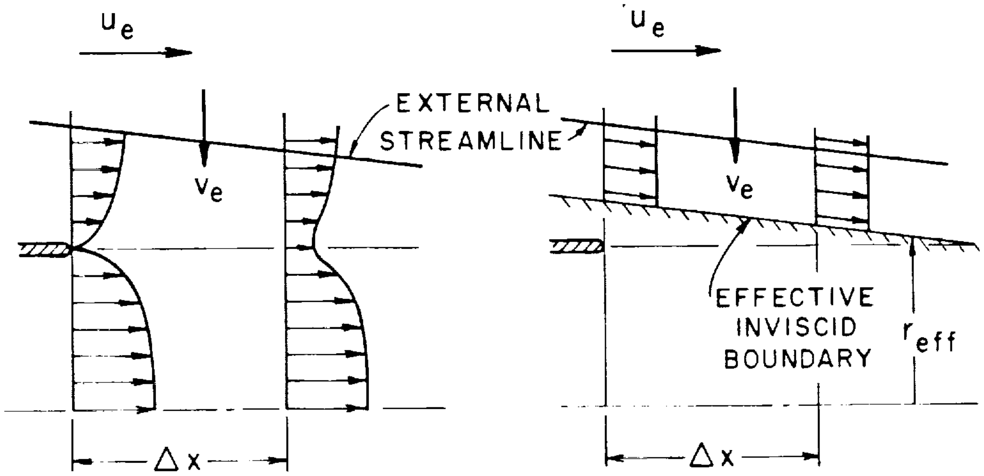

Figure 3.4 Effective boundary concept for an axisymmetric shear layer.

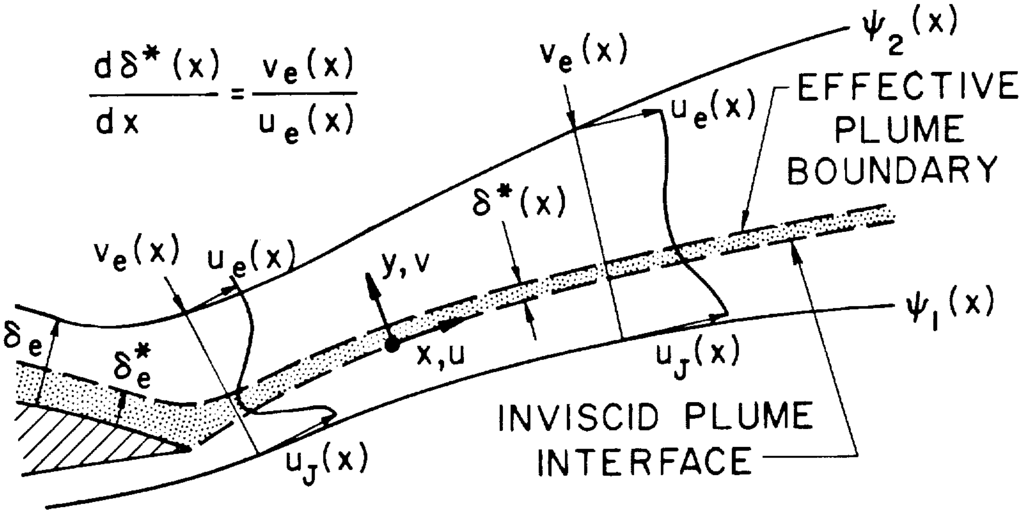

Figure 3.5 Addition of displacement thickness to inviscid plume interface yielding effective plume boundary.

The validity of the effective boundary concept can be demonstrated by a simple example, illustrated in Figure 3.6. Here, the plume is perfectly expanded and a constant pressure mixing calculation is performed in the absence of initial boundary layers. The outer edge normal velocity variation, $v_e(x)$, predicted by a BOAT calculation, was then integrated to determine $\delta^*(x)$ [via

Eq. (7)] yielding the illustrated effective plume geometry (obtained by adding $\delta^*(x)$ to the plume interface $r_j = 1.0$) . Performance of the inviscid external flow calculation over this geometry yielded a normal velocity distribution along the upper shear layer boundary which compared favorably with BOAT's predictions for $v_e(x)$, indicating a matching of the streamline slopes along this boundary. An accurate representation of the entrainment effect on the upstream inviscid flow is therefore expected. The slight disagreement at the initial shear layer region is produced by the numerical smoothing (in the inviscid code) of the effective shoulder in the boundary (i.e., the flow is forced to turn smoothly instead of the sudden turn predicted by BOAT). The slightly increasing difference between the inviscid and BOAT-calculated normal velocities, with increasing x , is attributed to prematurely terminating the effective body at $x/r_j \approx 3$ and employing a cylindrical boundary downstream.

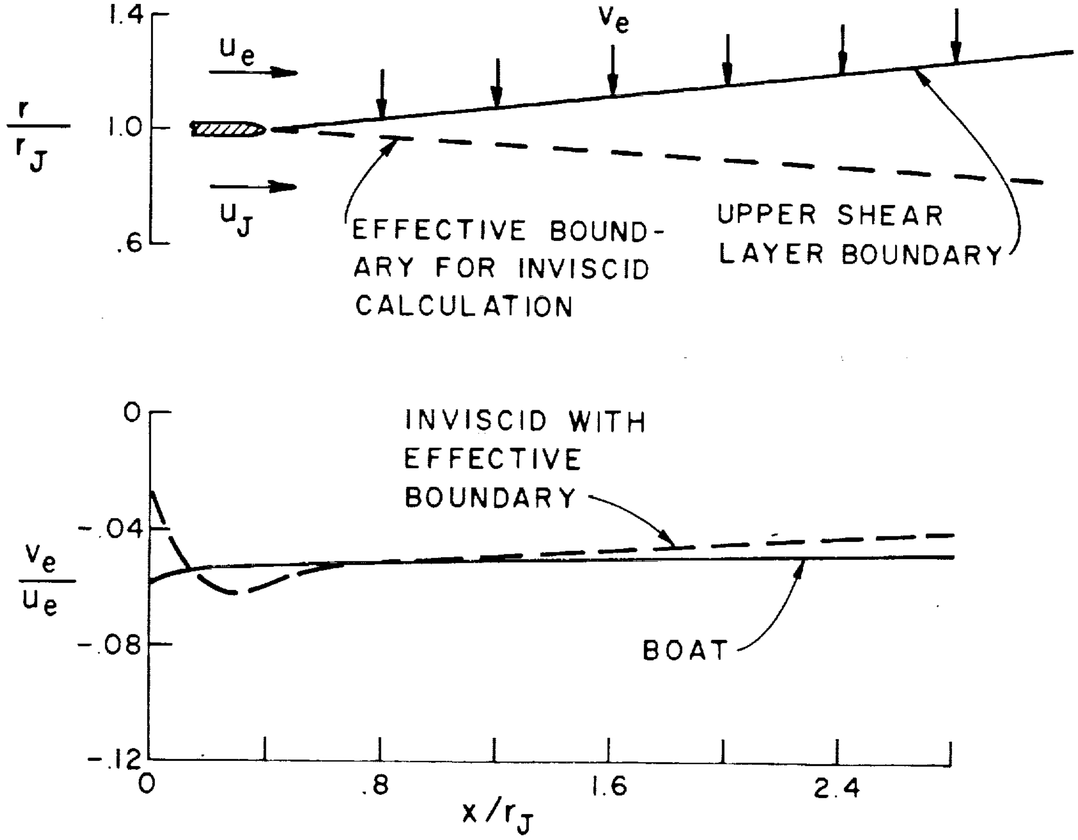

Figure 3.6 Comparison of effective entrainment velocity calculated with BOAT and with inviscid external flow code using effective boundary concept, $u_e/u_J = 0.2$, $M_e = 0.4$.

4. COMPUTATIONAL PROCEDURES

4.1 Integration Scheme

In BOAT, a parabolic system of equations [Eqs. (1) - (5)] are integrated in the axial direction from specified initial conditions $u(x_1,\psi)$, $T(x_1,\psi)$, $F_i(x_1,\psi)$, $k(x_1,\psi)$, and $\varepsilon(x_1,\psi)$ where x_1 is the initial axial station and $\psi_1 \le \psi \le \psi_2$ where $\psi_1(x_1)$ and $\psi_2(x_1)$ are the upper and lower mixing layer boundaries. A fixed number of grid points, (N) , are equally spread across the shear layer in intervals of $\Delta\psi = (\psi_2 - \psi_1)/(N-1)$.

Referring to Figure 4.1, the following steps are performed in integrating the flowfield equations from x_1 to x_2 $(= x_1 + \Delta x)$:

- The rate of mass entrainment is determined at the upper and lower boundaries at x_1 (see Section 4.6) and used to evaluate ψ_1 and ψ_2 at x_2 in an explicit fashion [i.e., $\psi_{1,2}(x_2) = \psi_{x_{1,2}}(x_1)\,\Delta x$].

- The dependent variables at the initial station x_1 are redistributed over the extended interval $\psi_1(x_2) \le \psi \le \psi_2(x_2)$ in equally spaced intervals of $\Delta\psi = [\psi_2(x_2) - \psi_1(x_2)]/(N-1)$.

- The equations are integrated along the streamlines $\psi(I) = \psi_1(x_2) + (I-1)/(N-1)*[\psi_2(x_2) - \psi_1(x_2)]$ for $I = 2$ to $N-1$, with edge conditions at $I = 1$ and $I = N$ specified, consistent with the inviscid flow pattern.

The sequential process above is then applied to advance the equations another integration step, etc., with the first step above performed at the point in the program where the calculated variables at x_2 are reset into the initial profile array.

4.2 Overlaid Procedure

In analyzing underexpanded plumes, the detailed inviscid exhaust/external flow solution is used to specify the variable edge conditions and pressure gradients for the subsequent shear layer analysis. The inviscid solutions are supplied to BOAT via arrays at arbitrary axial stations for both the exhaust and external flows. BOAT processes these data yielding orderly vector arrays in mapped stream-function (x,ω) coordinates, which eliminates the need for inviscid map searching procedures. Referring to Figure 3.2, the procedure is as follows:

- At axial stations X_K , the user supplies arrays of r_I , U_I , P_I , and T_I . For the jet exhaust flow, these arrays extend from the axis to the plume interface while for the external flow, they extend from the interface to an arbitrary location. The axial stations for the jet exhaust and external flow need not coincide.

- The program calculates the value of ψ at each point I via integration of Eq. (6) . For the jet exhaust data we have

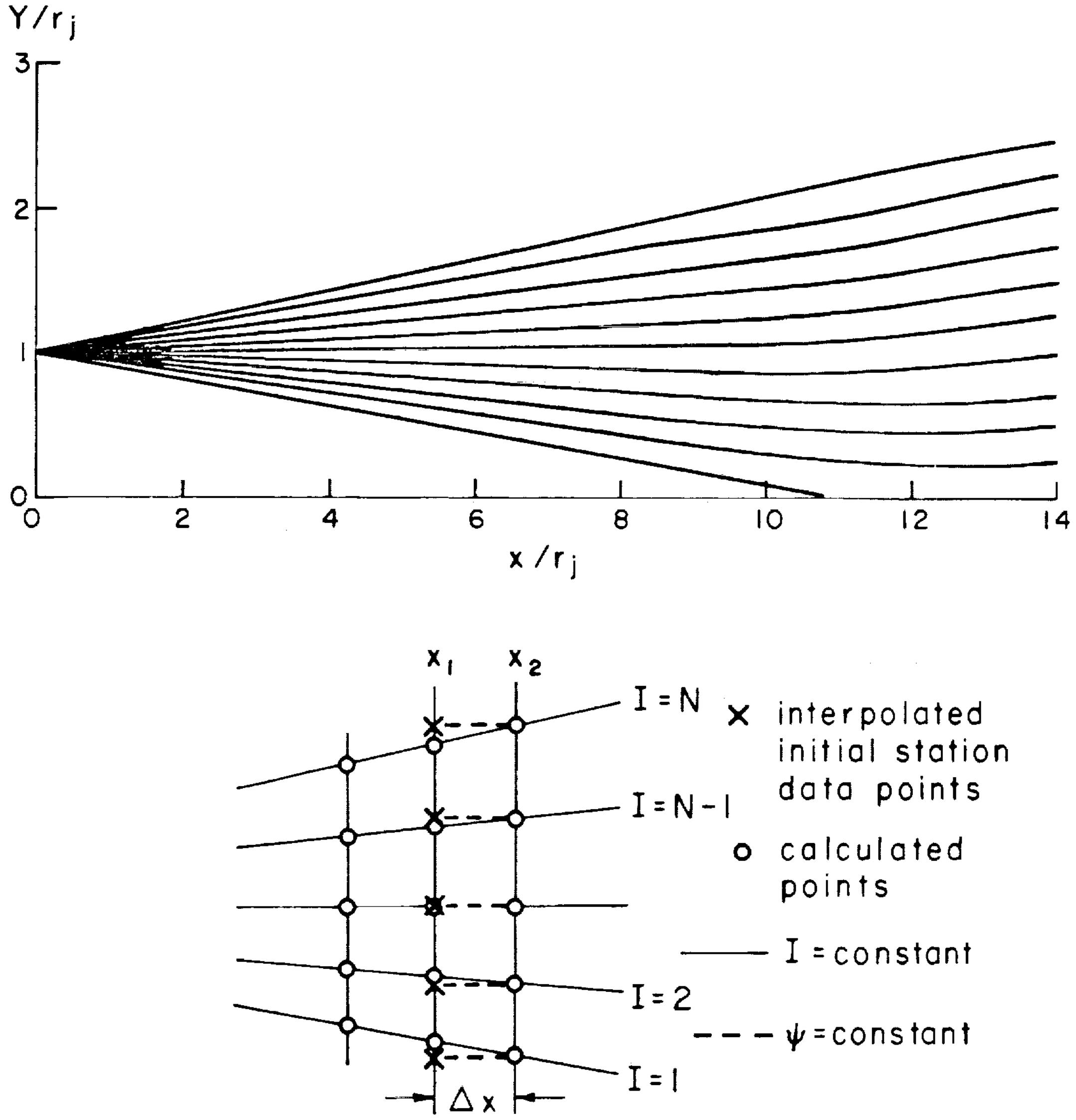

Marching procedure

Figure 4.1 Computational network.

$$\psi_I = \left(\int_o^{r_I} \rho_I U_I dr^2 \right)^{1/2} \tag{8a}$$

while for the external flow we obtain

$$\psi_I = \left(\psi_{jet}^2 + \int_{r_{jet}}^{r_I} \rho_I U_I dr^2 \right)^{1/2} \tag{8b}$$

where ψ_{jet} is a constant and r_{jet} is the local height of the plume interface at the axial station of interest.

- The value of nondimensional stream function ω is determined at each point I . For the jet exhaust, ω is given by

  $$\omega_I = \psi_I / \psi_{jet} \tag{9a}$$

  while for the external flow, by

  $$\omega_I = [\psi_I - \psi_{jet}]/[\psi_{ext}(x) - \psi_{jet}] \tag{9b}$$

  where $\psi_{ext}(x)$ is the variable value of ψ at the external flow upper data boundary.

- Vector arrays, equally spaced in ω $(0 \le \omega \le 1)$, are created for the jet exhaust and external flows of the form $VJET_{M,L,K}$ and $VEXT_{M,L,K}$. M designates the variable type $(1 = r\ ,\ 2 = P\ ,\ 3 = T$, and $4 = U)$, L designates the value of ω [$\omega = (L-1)/(L_{max}-1)$ where L_{max} is a fixed integer constant specified by the user for defining the grid definition in the mapped arrays], and I designates the axial station.

Since all jet or external profiles have the same number of mapped data points, L_{max} , radial map search procedures are also eliminated. Thus, properties at the lower shear layer boundary $\psi\ (x)$ are determined as follows:

- $\omega = \psi_1(x)/\psi_{jet}$ is determined yielding the index $L = \omega * (L_{max} - 1) + 1$ such that $\omega(L) \le \omega \le \omega(L+1)$.

- Properties $f_{M,K}$ are determined at the stations K and $K+1$ (where $x_K \leq x \leq x_{K+1}$) by the linear interpolation

$$f_{\substack{M,K\\K+1}} = \text{VECT}_{\substack{M,L,K\\K+1}} + R\psi\left(\text{VECT}_{\substack{M,L+1,K\\K+1}} - \text{VECT}_{\substack{M,L,K\\K+1}}\right) \qquad (10a)$$

  where $R\psi = \omega * (L_{max} - 1) - (L - 1)$ and VECT represents either VJET or VEXT.

- The desired properties f_M are determined by the interpolation

$$f_M = f_{M,K} + RX\left(f_{M,K+1} - f_{M,K}\right) \qquad (10b)$$

  where $RX = (x - x_K)/(x_{K+1} - x_K)$

For the external flow, the same approach is followed with ω in the first step above evaluated by the relation $\omega = [\psi_2(x) - \psi_{jet}]/[\psi_{ext}(x) - \psi_{jet}]$. It has been found most expeditious to evaluate the pressure gradients across the shear layer directly from the mapped arrays {i.e., $p_x(x,\psi_L) = [\text{VECT}\ (2, L, K+1) - \text{VECT}\ (2, L, K)]/(x_{K+1} - x_K)$ where $x_K < x < x_{K+1}$ and $\omega_L = \psi_L/\psi_{jet}$} for each individual streamline, ψ_L.

4.3 Finite Difference Formulation

4.3.1 <u>Equations</u>.- The same implicit/explicit formulation employed in the LAPP code[7] has been retained in BOAT. With the notation depicted in Figure 4.2

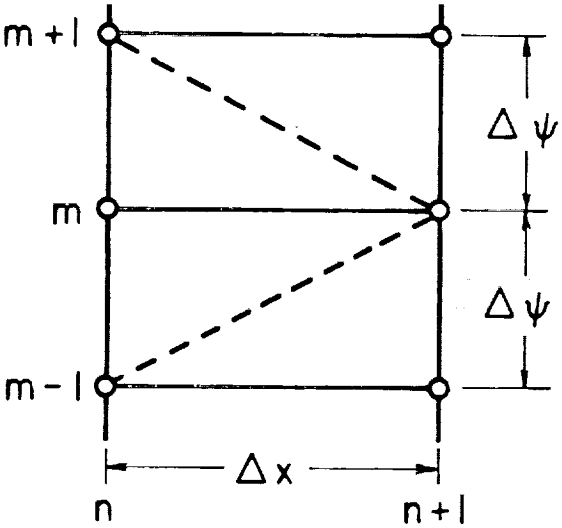

Figure 4.2 Finite difference index notation.

the resulting difference equations are written:

Species Diffusion

$$\left(F_i\right)_{n+1,m} = \left(F_i\right)_{n,m} + \frac{\Delta x}{\psi_m}\frac{\partial}{\partial\psi}\left[\frac{Le}{Pr}\,\frac{\mu\rho u r^2}{\psi}\left(F_i\right)_\psi\right]_{n,m} + \frac{\left(\dot{w}_i\right)_{n+1,m}\Delta x}{(\rho u)_{n,m}} \tag{11a}$$

and on the axis (m = 1) by

$$\left(F_i\right)_{n+1,1} = \left(F_i\right)_{n,1} + 2\Delta x\left(\frac{\mu Le}{Pr}\right)_{n,1}\frac{\partial}{\partial\psi}\left[\left(F_i\right)_\psi\right]_{n,1} + \frac{\left(\dot{w}_i\right)_{n+1,m}\Delta x}{(\rho u)_{n,1}} \tag{11b}$$

Axial Momentum

$$u_{n+1,m} = u_{n,m} + \frac{\Delta x}{\psi_m}\frac{\partial}{\partial\psi}\left(\frac{\mu\rho u r^2}{\psi}\,u_\psi\right)_{n,m} - \frac{\left(P_x\right)_{n+\frac{1}{2},m}\Delta x}{(\rho u)_{n,m}} \tag{12a}$$

and on the axis (m = 1) by

$$u_{n+1,1} = u_{n,1} + 2\Delta x(\mu)_{n,1}\frac{\partial}{\partial\psi}\left(u_\psi\right)_{n,1} - \frac{\left(P_x\right)_{n+\frac{1}{2},1}\Delta x}{(\rho u)_{n,1}} \tag{12b}$$

Energy

$$\begin{aligned} T_{n+1,m} = T_{n,m} &+ \frac{\Delta x}{\psi_m c_{p_{n,m}}}\frac{\partial}{\partial\psi}\left(\frac{c_p}{Pr}\,\frac{\mu\rho u r^2}{\psi}\,T_\psi\right)_{n,m} \\ &+ \frac{\left(P_x\right)_{n+\frac{1}{2},m}\Delta x}{\left(\rho c_p\right)_{n,m}} - \frac{\Delta x}{\left(\rho u c_p\right)_{n,m}}\sum_i\left(h_i\dot{w}_i\right)_{n,m} \\ &+ \left(\frac{\mu\rho u r^2}{c_p}\right)_{n,m}\frac{\Delta x}{\psi_m^2}\left[\frac{\partial}{\partial\psi}\left(u_\psi\right)_{n,m} + \left(\frac{Le}{Pr}\right)_{n,m}\left(T_\psi\right)_{n,m}\sum_i\left(c_{p_i}\right)_{n,m}\left(F_{i_\psi}\right)_{n,m}\right] \end{aligned} \tag{13a}$$

and on the axis (m = 1) by

$$T_{n+1,1} = T_{n,1} + 2\left(\frac{\mu}{Pr}\right)_{n,1} \frac{\partial}{\partial\psi}\left(T_\psi\right)_{n,1} + \frac{\left(P_x\right)_{n+\frac{1}{2},1}\Delta x}{\left(\rho c_p\right)_{n,1}} - \frac{1}{\left(\rho u c_p\right)_{n,1}}\sum\left(h_i\dot{w}_i\right)_{n,1} \tag{13b}$$

where first derivatives f_ψ are given by

$$\left(f_\psi\right)_{n,m} = \frac{f_{n,m+1} - f_{n,m-1}}{2\,\Delta\psi} \tag{14a}$$

and second derivatives of the form $\frac{\partial}{\partial\psi}\left(af_\psi\right)$ are given by

$$\frac{\partial}{\partial\psi}\left(af_\psi\right)_{n,m} = a_{n,m+\frac{1}{2}}\frac{\left(f_{n,m+1} - f_{n,m}\right)}{\Delta\psi^2} - a_{n,m-\frac{1}{2}}\frac{\left(f_{n,m} - f_{n,m-1}\right)}{\Delta\psi^2} \tag{14b}$$

where $a_{n,m\pm\frac{1}{2}} = \dfrac{a_{n,m} + a_{n,m\pm1}}{2}$

The pressure gradient $\left(P_x\right)_{n+\frac{1}{2},m}$ is given by

$$\left(P_x\right)_{n+\frac{1}{2},m} = \frac{P_{n+1,m} - P_{n,m}}{\Delta x} \tag{15}$$

The above equations are of first order accuracy in Δx and second order accuracy in $\Delta\psi$. Analogous expressions result for the turbulence equations for k and ϵ.

4.3.2 Linearization of chemistry terms.- The species mole fractions at station $n+1,m$ are determined from the species conservation equations by linearizing the chemistry terms [i.e., $(\dot{w}_i)_{n+1,m}$] and inverting the resulting matrix. The linearizations involving species F_i and F_j (for a two-body reaction) or F_i, F_j, and F_k (for a three-body reaction) at station $n+1$ (all variables are known at station n) are given by

$$\begin{aligned}\left(F_iF_j\right)_{n+1} &= \left(F_iF_j\right)_n + F_{jn}\left[\left(F_i\right)_{n+1} - \left(F_i\right)_n\right] + F_{in}\left[\left(F_j\right)_{n+1} - \left(F_j\right)_n\right] \\ &= -\underline{\underline{\left(F_iF_j\right)_n}} + \underline{\left(F_j\right)_n}\left(F_i\right)_{n+1} + \underline{\left(F_i\right)_n}\left(F_j\right)_{n+1}\end{aligned} \tag{16a}$$

$$\begin{aligned}\left(F_iF_jF_k\right)_{n+1} = -\underline{\underline{2\left(F_iF_jF_k\right)_n}} &+ \underline{\left(F_jF_k\right)_n}\left(F_i\right)_{n+1} \\ &+ \underline{\left(F_iF_k\right)_n}\left(F_j\right)_{n+1} + \underline{\left(F_iF_j\right)_n}\left(F_k\right)_{n+1}\end{aligned} \tag{16b}$$

The terms underscored by a single line contribute to the elements of the coefficient matrix, while the terms underscored by a double line contribute to the known column matrix on the right-hand side of the matrix equation for the linearized system. Thus, the matrix equation takes the form (for N species):

$$\begin{bmatrix} a_{11} & a_{12} & a_{13} & & a_{1N} \\ a_{21} & & & & \\ & & & & \\ & & & & \\ a_{N1} & & & & a_{NN} \end{bmatrix} \begin{bmatrix} F_1 \\ F_2 \\ \\ \\ F_N \end{bmatrix} = \begin{bmatrix} Q_1 \\ Q_2 \\ \\ \\ Q_N \end{bmatrix} \tag{17}$$

4.3.3 Allowable step size.- The maximum allowable marching step must satisfy explicit stability considerations for a parabolic system of equations as well as those of overall accuracy. As such, it is taken to be the minimum value of

$$\Delta x = \left(\frac{\psi^2 \mathrm{Pr}}{2\mathrm{Le}\mu\rho u r^2}\right)_{n,m} \Delta\psi^2 \tag{18a}$$

and

$$\Delta x = y_{n,m} - y_{n,m-1} \tag{18b}$$

as evaluated for all grid points m at station n . On the axis $(m = 1)$, Eq. (18a) is replaced by

$$\Delta x = \left(\frac{\mathrm{Pr}}{4\mu\mathrm{Le}}\right)_{n,m} \Delta\psi^2 \tag{19}$$

The chemistry terms impose no stability limitation on the step size due to their implicit formulation. To insure an accurate description of chemical processes when the chemistry is "fast" (i.e., when one or more reactions are near equilibrium), a maximum allowable temperature change, ΔT_{max}, is permitted along a streamline in an integration step. The value of ΔT_{max} is input to the code. Should the temperature change exceed this value, the step size is repeatedly halved until the temperature change is less than ΔT_{max}, or the step size becomes less than a user input minimal step, in which case the program terminates. Should the user input too large a value of ΔT_{max} for the case considered, the computed species mole fractions can become negative in "fast" chemistry regions. This is also handled by step size halving until the predicted mole fractions are all positive. The choice of $\Delta T_{max} = 5°K$ should suffice in the most stringent situations, but may be overly limiting in general (i.e., with a coarse grid, such changes could occur in a given step due solely to diffusive processes). In nonreactive situations, or situations where rapid burning is not anticipated, a value of $\Delta T_{max} = 25°K$ may be more appropriate.

4.4 Chemical Reaction Rate Equations

Ten possible reaction types are included in the program:

Reaction Type	
(1)	$A + B \rightleftarrows C + D$
(2)	$A + B + M \rightleftarrows C + M$
(3)	$A + B \rightleftarrows C + D + E$
(4)	$A + B \rightleftarrows C$
(5)	$A + M \rightleftarrows C + D + M$
(6)	$A + B \rightarrow C + D$
(7)	$A + B + M \rightarrow C + M$
(8)	$A + B \rightarrow C + D + E$
(9)	$A + B \rightarrow C$
(10)	$A + M \rightarrow C + D + M$

Reaction types (6)-(10) correspond to reaction types (1)-(5), but proceed in the forward direction only. In reactions (2), (5), (7), and (10), M is an arbitrary third body. In this program, all species are assumed to have equal third body efficiencies; thus, in evaluating $\dot{w}^{(j)}$, $F_M = (W)^{-1}$. The formulation for the net rates of production for each reaction type is written below.

$$(1) \qquad \dot{w}^{(j)} = k_f \rho^2 F_A F_B - \frac{k_f \rho^2 F_C F_D}{K_p}$$

$$(2) \qquad \dot{w}^{(j)} = \frac{k_f \rho^3 F_A F_B}{W} - \frac{k_f \rho^2 F_C}{K_p WRT}$$

$$\dot{w}^{(j)} = k_f \rho^2 F_A F_B - \frac{k_f \rho^3 F_C F_D F_E RT}{K_p} \tag{3}$$

$$\dot{w}^{(j)} = k_f \rho^2 F_A F_B - \frac{k_f \rho F_C}{K_p RT} \tag{4}$$

$$\dot{w}^{(j)} = \frac{k_f \rho^2 F_A}{W} - \frac{k_f \rho^3 F_C F_D RT}{K_p W} \tag{5}$$

$$\dot{w}^{(j)} = k_f \rho^2 F_A F_B \tag{6}$$

$$\dot{w}^{(j)} = \frac{k_f \rho^3 F_A F_B}{W} \tag{7}$$

$$\dot{w}^{(j)} = k_f \rho^2 F_A F_B \tag{8}$$

$$\dot{w}^{(j)} = k_f \rho^2 F_A F_B \tag{9}$$

$$\dot{w}^{(j)} = \frac{k_f \rho^2 F_A}{W} \tag{10}$$

The forward rate coefficient, k_f , is expressed in the form,

$$k_f = AT^{-N} \exp (B/RT) \tag{20}$$

and K_p is determined from

$$\ln K_p = - \Delta G/RT \tag{21}$$

The rate coefficients are divided into eight types:

Rate Coefficient Type	
(1)	$k_f = A$
(2)	$k_f = AT^{-1}$
(3)	$k_f = AT^{-2}$
(4)	$k_f = AT^{-\frac{1}{2}}$
(5)	$k_f = A \exp (B/RT)$
(6)	$k_f = AT^{-1} \exp (B/RT)$
(7)	$k_f = AT^{-\frac{3}{2}}$
(8)	$k_f = AT^{-N} \exp (B/RT)$

4.5 Turbulence Model

4.5.1 Mixing length model.- In the extended ML model employed in BOAT, the turbulent viscosity, μ_t , at all interior points is given by the expression

$$\mu_t = \rho \ell^2 \left| \frac{\partial u}{\partial y} \right| \tag{22a}$$

and on the axis by

$$\mu_t = \rho \ell^3 \left| \frac{\partial^2 u}{\partial y^2} \right| \tag{22b}$$

In application of this model, the mixing length ℓ is linearly related to the mixing layer thickness δ , i.e., ℓ/δ = constant . Several definitions of δ are illustrated in Figure 4.3. We have attempted to achieve some degree of generality by the use of just two scaling constants (a nearfield, two-dimensional constant and a farfield, axisymmetric constant). No further empirical relations are employed. The scaling constants, ℓ/δ , were determined by carefully matching the fundamental experimental data to be discussed in Section 5.

$$\text{Turbulent Viscosity: } \mu_t = \rho \ell^2 \left| \frac{\partial u}{\partial y} \right|$$

$$\text{on axis: } \mu_t = \rho \ell^3 \left| \frac{\partial^2 u}{\partial y^2} \right|$$

Length Scale: $\ell = .082\,\delta$ for all flows

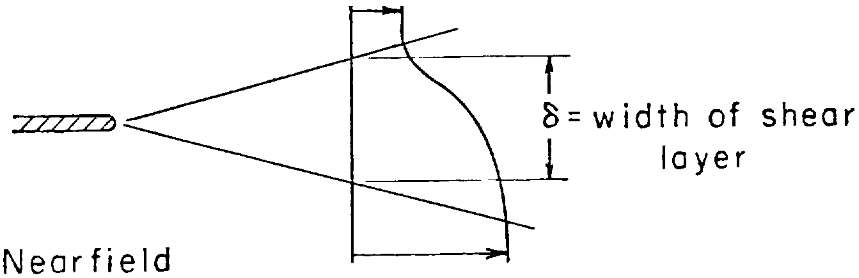

Nearfield

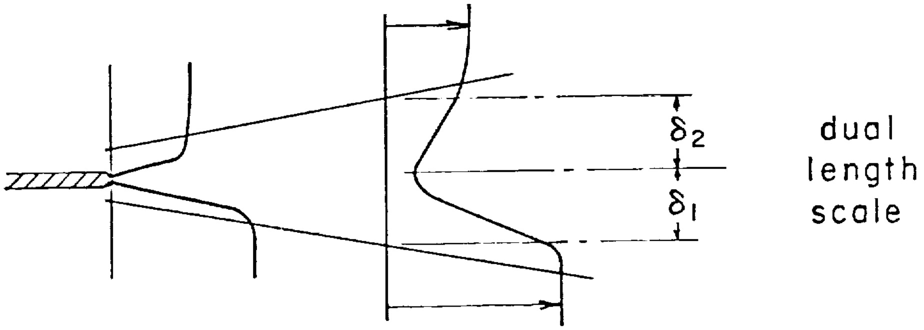

Nearfield with boundary layers

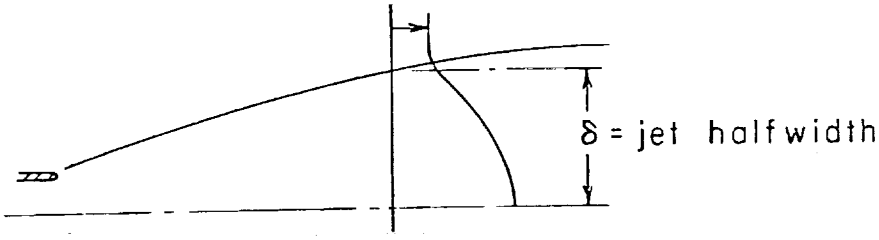

Farfield

Figure 4.3 Characteristic mixing layer thickness.

In application of this model in x,ψ coordinates, at an interior point n,m we employ

$$\mu_{t_{n,m}} = \frac{\left(\rho^2 ur\right)_{n,m}}{\psi_m} \ell^2 \left(u_\psi\right)_{n,m} \tag{23a}$$

while at the axis, the relation

$$\mu_{t_{n,1}} = 2\rho_{n,1}\ell^3 \frac{\left(u_{n,2} - u_{n,1}\right)}{\left(y_{n,2}\right)^2} \tag{23b}$$

is employed.

4.5.2 Two-equation model*.- The kε2 model, developed by the group at the Imperial College[15], has been incorporated in the BOAT code. Here, the turbulent viscosity is given by

$$\mu_t = C_\mu \rho \frac{k^2}{\varepsilon} \tag{24}$$

where C_μ and the constants C_1, C_2, σ_k, and σ_ε have been extracted directly from Reference 15. As in the ML model, the constants differ for nearfield (2D) and farfield (axisymmetric) situations. These constants are summarized below:

$$C_\mu = 0.09\, g\, \overline{(P/\varepsilon)} - 0.0534\, f$$

$$C_1 = 1.4$$

$$C_2 = 1.94 - .1336\, f$$

$$\sigma_k = 1.0$$

$$\sigma_\varepsilon = 1.3$$

$$f = \left[\frac{y_{1/2}}{u_c} \left|\frac{du_c}{dx}\right| - \frac{du_c}{dx}\right]^{.2}$$

where $\overline{P/\varepsilon}$ (P is the turbulence production rate) is the shear stress weighted average across the mixing region. The functional dependence of g on $\overline{P/\varepsilon}$ and of f on the axial velocity centerline decay follow Reference 15 directly. In this regard it is important to note that the axisymmetric correction term,

---

* The incorporation of the kε2 turbulence model into the BOAT code and its subsequent validation by comparison with experimental data (see Section 5) was supported by the Naval Weapons Center under Contract No. N00123-78-C-0010.

f , was obtained by matching data on constant pressure, nonreacting coaxial jets. For generalized plume studies where the centerline velocity additionally changes due to both pressure gradients and chemistry effects, it may be necessary to isolate the diffusive decay effect by use of a "dummy" inert species. Several new approaches[16,17] (which do not depend on the centerline decay) for extending kε2 models to axisymmetric flows are presently being investigated and should lead to a greater degree of generality in application of this model to complex flow situations.

4.6 Shear Layer Growth

The smooth growth of the shear layer is provided for by the use of rules dependent upon the profile variations near the edges. A certain amount of trial and error has been exercised in arriving at rules which are generally satisfactory. Following the approach of Patankar and Spalding[8], we start with the limiting expression

$$\dot{m} = \lim_{u_y \to 0} \frac{1}{y} (\mu_t\, y\, u_y)_y / u_y \tag{25}$$

for the local rate of mass entrained at the shear layer edges ψ_1 and ψ_2 . With the velocity variation near the edges approximated by the expression

$$u(y) = u_{1,2} + c(y - y_{1,2})^2 \tag{26}$$

and using the mixing length expression for μ_t we obtain

$$\dot{m}_{n,1} = 4\rho_{n,1}\ell^2 \; (u_{n,2} - u_{n,1})/(y_{n,2} - y_{n,1})^2 \tag{27a}$$

at the lower boundary, $m = 1$, and

$$\dot{m}_{n,N} = 4\rho_{n,N}\ell^2 \; (u_{n,N} - u_{n,N-1})/(y_{n,N} - y_{n,N-1})^2 \tag{27b}$$

at the upper boundary, $m = N$. These relations are applied in an explicit fashion in predicting the values of the stream function $\psi_{1,2}$ at $x + \Delta x$. Thus,

$$\psi_1(x + \Delta x) = \psi_1(x) + \left(\frac{\dot{m}r}{\psi}\right)_{n,1} \Delta x \tag{28a}$$

and

$$\psi_2(x + \Delta x) = \psi_2(x) + \left(\frac{\dot{m}r}{\psi}\right)_{n,N} \Delta x \tag{28b}$$

For the kε2 model, the shear layer growth at the upper boundary, ψ_2 , is estimated by the expression

$$\psi_2(x+\Delta x) = \psi_2(x) + 3r_{n-2}\,\mu_{t_{n-1}}\left(\frac{r_N - r_{N-2}}{r_N - r_{N-1}}\right) \tag{29}$$

with a similar expression employed in estimating the growth rate at the lower (ψ_1) boundary.

4.7 Initialization Procedures

Three options are provided in BOAT for initiating the mixing layer calculation; namely, a generalized option where the user specifies initial profiles, a shear layer option, and a boundary layer option.

4.7.1 Generalized option.- In this mode, schematized in Figure 4.4, the user inputs values of the dependent variables u and T , and the mole fractions* X_i , as a function of radial distance from the axis at an arbitrary x initial station. The point $I=1$ is either the lower edge of the shear layer, $\psi_{1(x)}$, or the axis, while the point $I=N$ is the upper mixing layer boundary. In using this option in conjunction with the overlaid procedure, the edge conditions (at $I=1$ and N) must be consistent with the inviscid flow solutions as defined by the exhaust and external flow maps.

After reading in the data indicated in Figure 4.4, the mass flow variable is determined at all points I and an equally spaced profile in $\Delta\psi$ is generated, where

$$\Delta\psi = (\psi_N - \psi_1) \,/\, (N-1) \tag{30}$$

Thus, the N specified data points, input in arbitrary intervals in the physical plane, are recast into an equally spaced array of N points in the transformed plane. The same number of grid points, N , is retained throughout the overall calculation.

The generalized option should always be implemented when the initial profiles are known. This, however, is not usually the case, and the options presented below can be utilized to yield code generated initial profiles. The code also has a restart option which allows for marching to a specified axial station and restarting from that point with no additional input requirements.

4.7.2 Shear layer option.- In this mode, schematized in Figure 4.5, a fully developed turbulent shear layer is assumed to exist at the starting station. For use in an overlaid approach, the user need specify only the composition of the jet and external streams, and the starting location x . Local

---

*It should be noted that while the user inputs the composition in terms of X_i , the integration is performed in terms of the dependent variable F_i , where $F_i = X_i/W$ and W is the local mixture molecular weight.

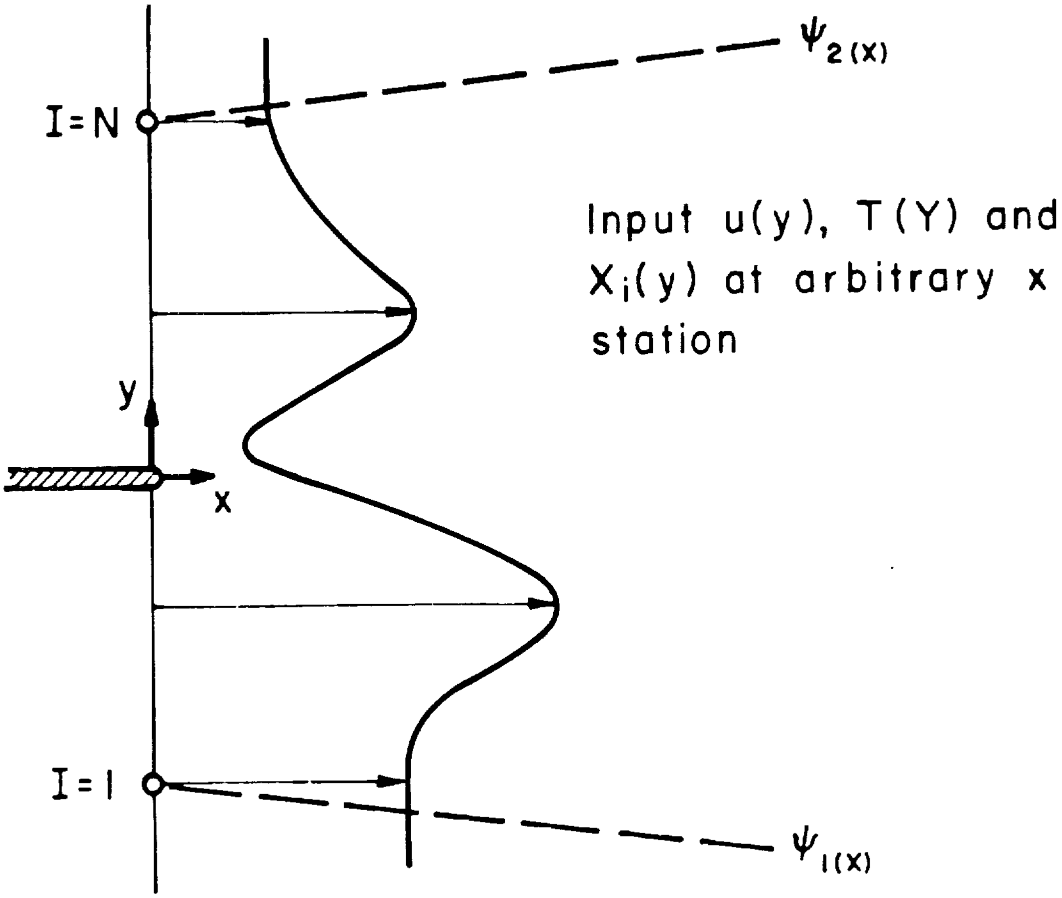

Figure 4.4 Arbitrary initial profile

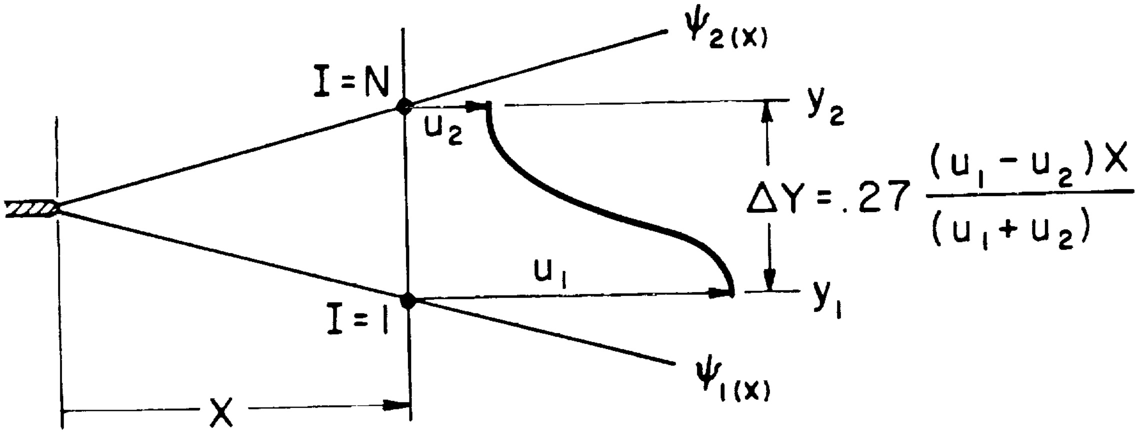

Figure 4.5 Shear layer initialization.

edge properties will be determined from the inviscid data maps. In the constant pressure mode, the velocity and temperature of the jet and external streams will additionally be required.

For most situations of interest, the initial shear layer width can be reasonably estimated by the incompressible relation[18]

$$y_2 - y_1 = .27 \frac{\left(u_1 - u_2\right)}{\left(u_1 + u_2\right)} x \tag{31}$$

where 1 and 2 designate the lower and upper shear layer boundaries. Properties are then distributed across the layer in accordance with the simple cubic relations

$$\frac{u - u_1}{u_2 - u_1} = \frac{T - T_1}{T_2 - T_1} = \frac{F_i - F_{i_1}}{F_{i_2} - F_{i_1}} = 3\eta^2\left(1 - \frac{2}{3}\eta\right) \tag{32}$$

where $\eta = (y - y_1)/(y_2 - y_1)$. The shear layer is centered about the plume interface and grid points are evenly spaced across it in increments of $\Delta\psi = (\psi_2 - \psi_1)/(N - 1)$.

4.7.3 Boundary layer option.- In the jet entrainment problem, the displacement effect of the external and nozzle boundary layers must be accurately accounted for in the initialization process as will be evident from the discussion presented in the next section. In this initialization option, schematically depicted in Figure 4.6, the user is required to supply values of the displacement thicknesses $\delta^*_{1,2}$ and nondimensional frictional velocities $u^*_{1,2}/u_{1,2}$ at the nozzle lip. The velocity profile used in the boundary layers is given by (see Reference 19, pp. 690-707)

$$\frac{u_{1,2} - u_{(\xi)}}{u^*_{1,2}} = - 2.5 \ln \xi + 1.38 \left[2 - w_{(\xi)}\right] \tag{33}$$

where Cole's universal wake function $w_{(\xi)}$ is well approximated by

$$w_{(\xi)} = 1 + \sin\left(\frac{2\xi - 1}{2}\right)\pi \tag{34}$$

Here, ξ is the nondimensional variable

$$\xi = |r - r_c|/\delta_{1,2} \tag{35}$$

and the frictional velocities $u^*_{1,2}$ are related to the wall shear stress by

$$\frac{u^*_{1,2}}{u_{1,2}} = \frac{\tau_{w_{1,2}}}{(\rho u)_{1,2}} = \frac{1}{Re_{1,2}}\left(\frac{\partial u}{\partial y}\right)_{w_{1,2}} \tag{36}$$

where Re is the Reynolds number per unit length. A nominal value of $u^*/u_{1,2} = 1/30$ is built into the code as a default option for users not supplying this information.

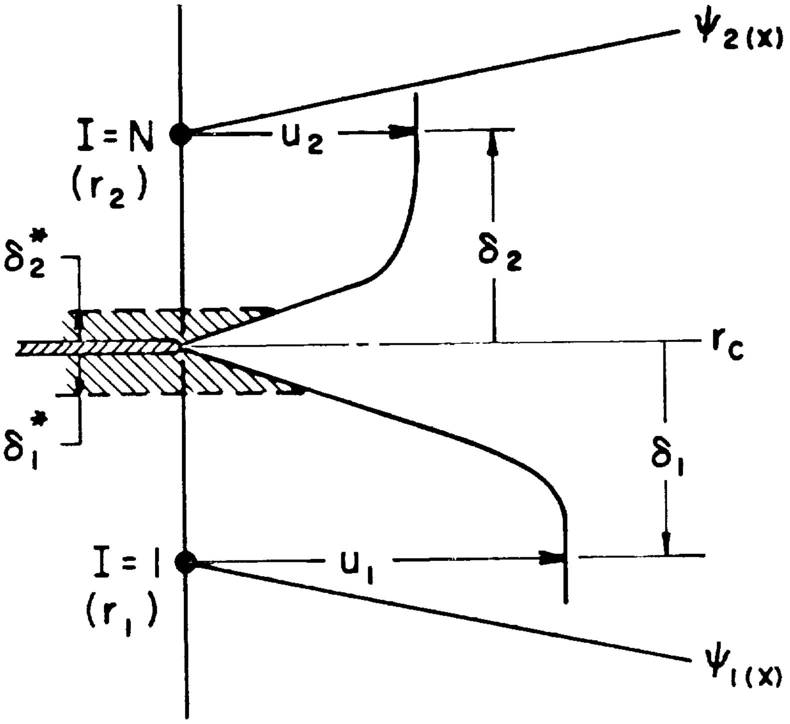

Input δ_1^* and δ_2^*

program determines

$$r_{1,2} = r_c \pm \delta_{1,2}$$

using velocity profile

$$\frac{u_{1,2} - u}{u^*_{1,2}} = -2.5 \ln \xi - 1.38 \left[2 w_{(\xi)} \right]$$

where $\xi = |r - r_c| / 2\delta_{1,2}$

Figure 4.6 Boundary layer initialization.

The temperature variation across the boundary layers is given by the Crocco relation, which for a Prandtl number of unity and insulated walls, is given by

$$\frac{T(\xi)}{T_{1,2}} = 1 + \frac{(\gamma_{1,2} - 1)}{2} M_{1,2}^2 \left[1 - \frac{u^2(\xi)}{u_{1,2}}\right] \tag{37}$$

If the boundary layer thickness is small in comparison with the nozzle exit radius, $\delta_{1,2}$ are readily obtained by the relations

$$\frac{\delta_{1,2}^*}{\delta_{1,2}} = \int_0^1 \left[1 - \frac{u(\xi)}{u_{1,2}} \frac{T_{1,2}}{T(\xi)}\right] d\xi \tag{38}$$

For thick boundary layers, we start with the expression

$$\delta_{1,2}^* = \frac{1}{r_j} \int_{r_j}^{r_j+\delta_{1,2}} \left(1 - \frac{u}{u_{1,2}} \frac{T_{1,2}}{T}\right) rdr \tag{39}$$

and after some manipulation, obtain

$$\frac{\delta_{1,2}}{r_j} = \frac{-I_1 + \sqrt{I_1^2 + 2I_2\left(\delta_{1,2}^{*2}/r_j^2 + 2\delta_{1,2}^*/r_j\right)}}{2I_2} \tag{40}$$

where

$$I_1 = \pm \int_0^1 \left(1 - \frac{u}{u_{1,2}} \frac{T_{1,2}}{T}\right) d\xi$$

$$I_2 = \pm \int_0^1 \left(1 - \frac{u}{u_{1,2}} \frac{T_{1,2}}{T}\right) \xi d\xi$$

4.7.4 kε2 initialization.- In the absence of any information regarding initial turbulence levels, the initial profiles of k and ε are obtained from the mixing length model based upon the relevant mean flow profiles. The ML model relates the turbulent shear stress $\rho\ u'v'$ to the local velocity gradient through the relation

$$\rho\ \overline{u'v'} = \rho\ \ell^2 \left(\frac{\partial u}{\partial y}\right) \left|\frac{\partial u}{\partial y}\right| \tag{41}$$

With the estimate that $k = |\overline{u'v'}|/0.3$,

$$k(y) = \frac{\mu_t(y)\ |\partial u/\partial y|}{0.3\rho(y)} \tag{42}$$

and assuming that $\overline{P/\varepsilon} \approx 1$, we obtain

$$\varepsilon(y) = \frac{0.09\rho(y)k^2(y)}{\mu_t(y)} \tag{43}$$

5. CODE VALIDATION

5.1 Incompressible Free Shear Layers

The validation process for BOAT was initiated with the analysis of two-dimensional incompressible free shear layers. Any code must demonstrate its ability to correctly predict this basic flow before being utilized in more complex situations. In performing these shear layer calculations, the ratio of ℓ/δ in the Prandtl mixing length model was varied and comparisons were made with experimental data to "calibrate" the model. The experimental data are generally given in terms of the spreading parameter, σ , as defined by the relation

$$\sigma = \frac{1.855\ \Delta x}{(\Delta y)_{.1 \rightarrow .9}} \tag{44}$$

where $(\Delta y)_{.1 \rightarrow .9}$ is the change in shear layer width over the distance Δx ; the shear layer width is defined as the distance between the points where $(u - u_2)/(u_1 - u_2) = .1$ and $.9$. This nomenclature is illustrated in Figure 5.1.

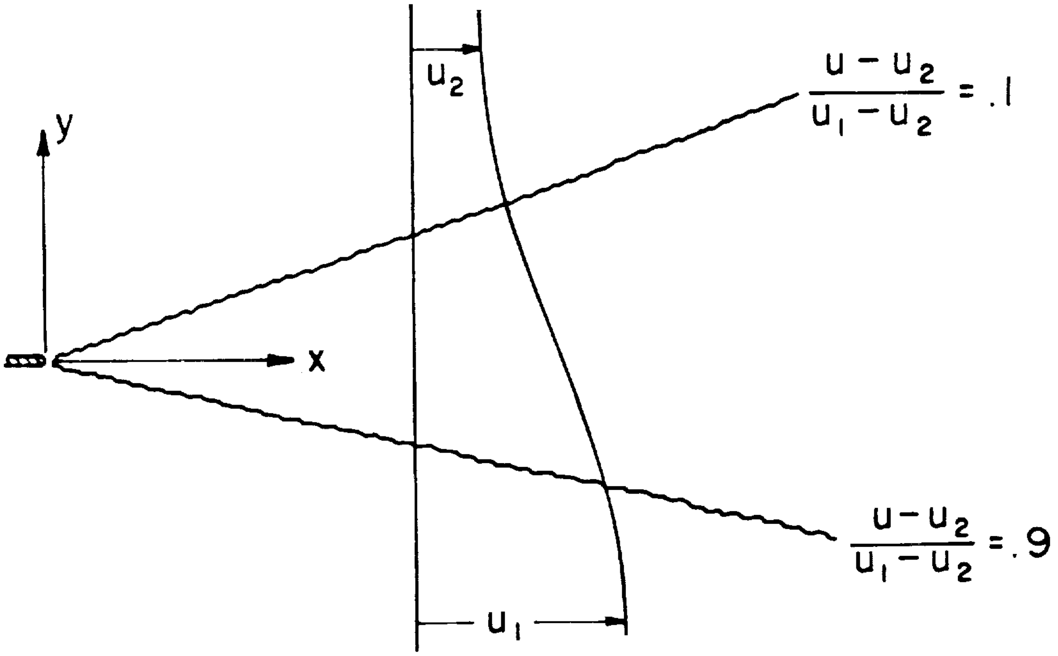

Figure 5.1 Spreading parameter nomenclature.

Results obtained from BOAT using both the ML and kε2 turbulence models are compared with spread rates from various investigators in Figure 5.2 .

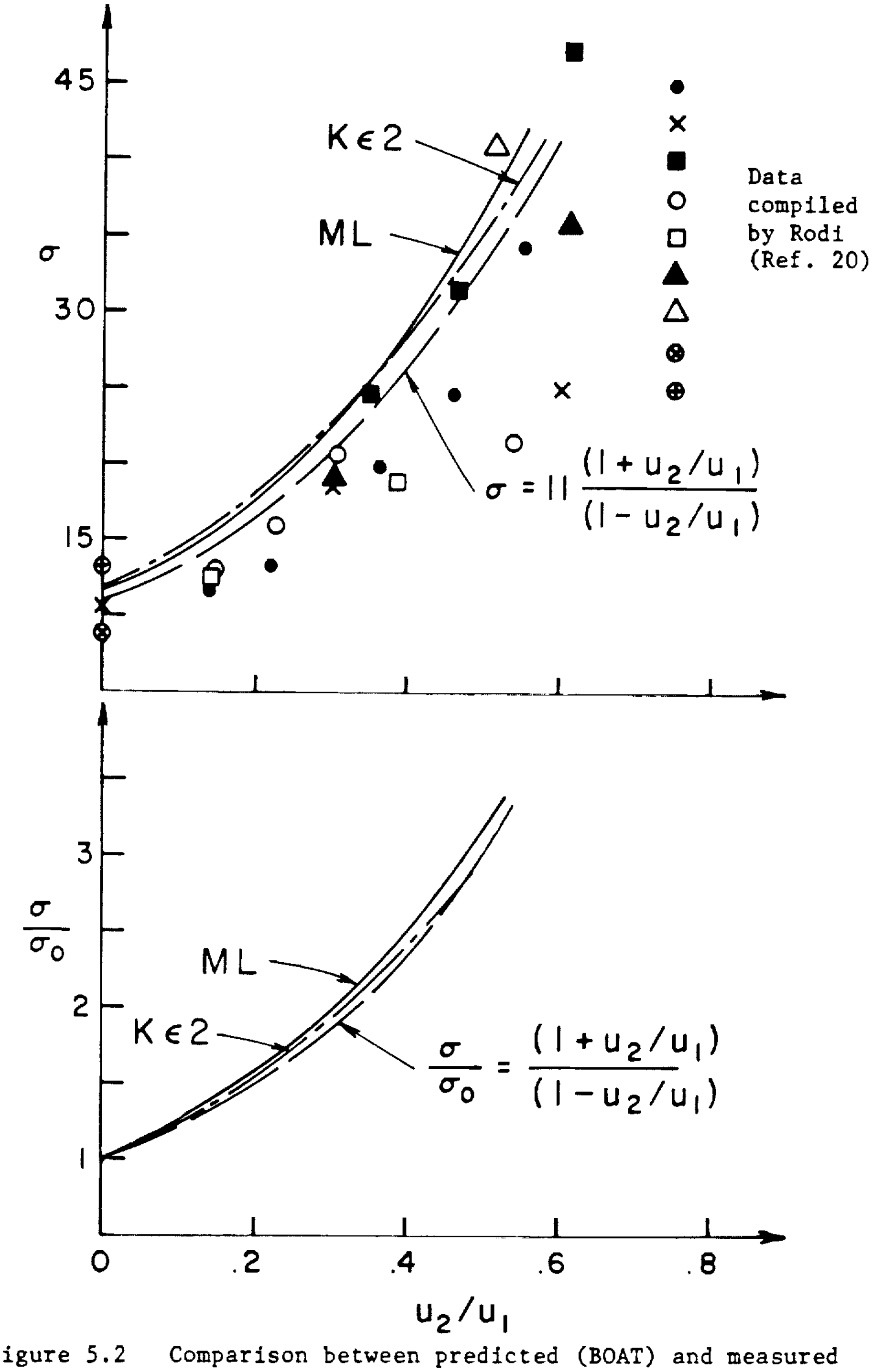

Figure 5.2 Comparison between predicted (BOAT) and measured (spread rates) two-dimensional shear layers.

The data were compiled and reviewed by Rodi[20], the relatively large spread in the data being attributed to varying turbulence levels in the free streams. The higher values of σ (smaller spread rates) correspond to the smaller free stream turbulence levels. Since the shear layer boundary conditions are based upon zero free stream turbulence, the predictions should match these higher values. Figure 5.2 shows that both the kε2 and ML model (with ℓ/δ = .065) predictions are in good agreement with these data. In terms of profile shapes, both the kε2 and ML models adequately predict both the velocity and turbulent shear stress profiles as illustrated in Figures 5.3a and b.

5.2 Incompressible Free Shear Layers with Initial Boundary Layers

The ability of BOAT to analyze an initially nonsimilar mixing region has been assessed by performing Test Case 4 of the NASA Shear Flow Conference[13,21]. In this case, two streams are initially separated by a symmetric airfoil with a 10° trailing edge, and initial profile data is supplied at a station 0.1 cm downstream of the trailing edge. The dual length scale approach in the ML model is required in this situation. The initial velocity profile data are depicted in Figure 5.4 (a), and comparisons of BOAT code velocity profile predictions with the data at a number of downstream stations are presented in Figures 5.4(b) through 5.4(h), respectively. The BOAT calculation was performed with a 31-point grid and the ratio of ℓ/δ in the Prandtl mixing length model set equal to 0.65. The results in the nonsimilar initial region (i.e., $x \le 25$ cm) are considered to be reasonable while those downstream are quite good.

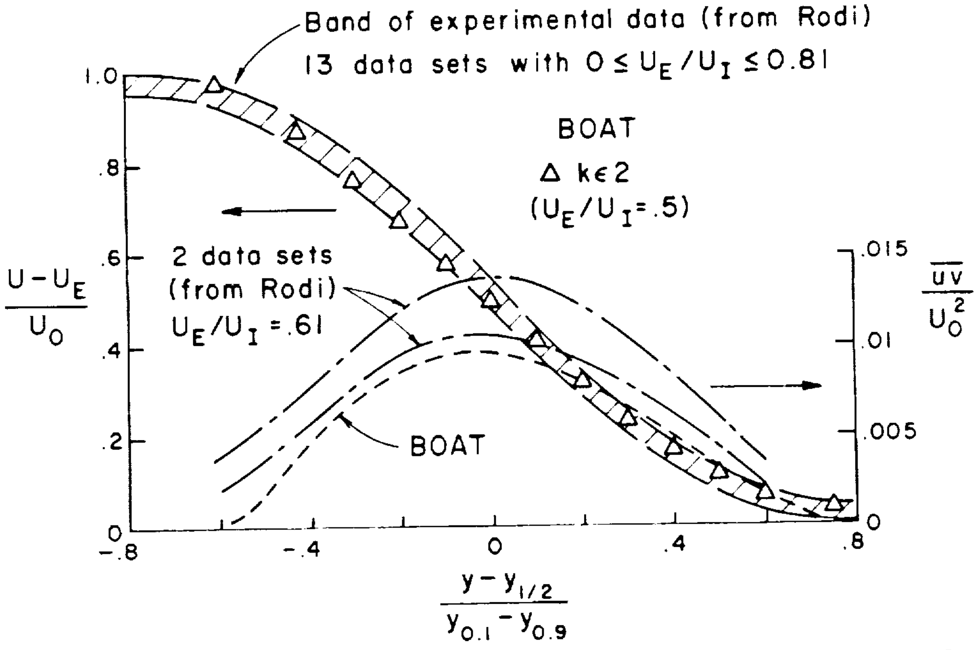

Figure 5.3a Comparison between predicted (BOAT) and measured velocity and shear stress profile for two-dimensional shear layers, kε2 model.

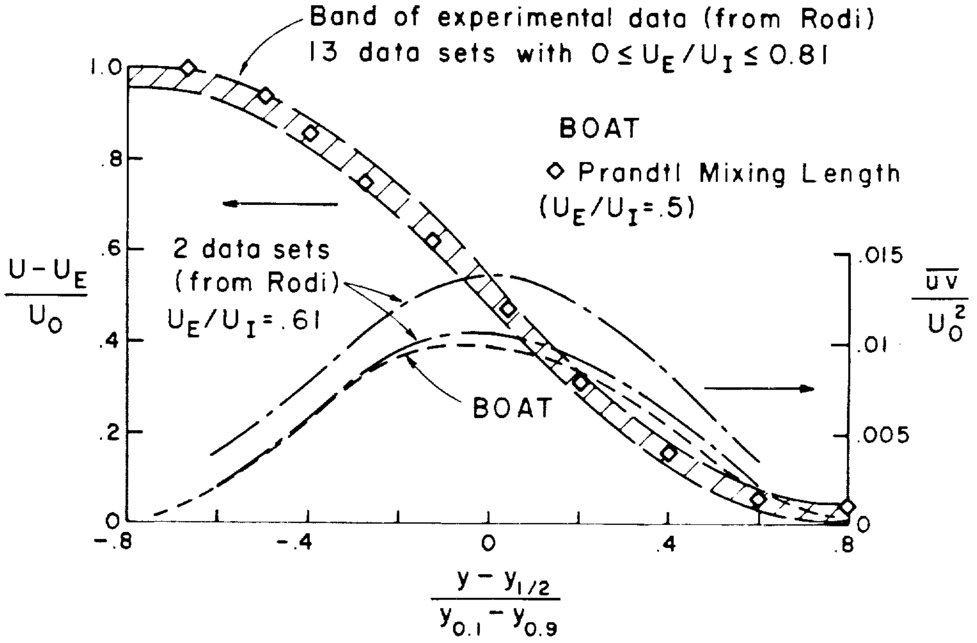

Figure 5.3b Comparison between predicted (BOAT) and measured velocity and shear stress profile for two-dimensional shear layers, Prandtl mixing length model.

In Figure 5.5, the predicted velocity profiles obtained with BOAT employing both the ML and kε2 models are compared with the Lee data at 12.7 cm as well as with ML and kε2 predictions by Launder et al.[15] and ML predictions by Rudy and Bushnell[22]. The BOAT ML predictions and both kε2 predictions fit the data quite well. The ML predictions of both Launder and Rudy do not pick up the velocity-defect region at all. Similar trends regarding the predictive capability of each model are observed in Figure 5.6, which compares predicted and measured shear stress profiles. At x = 76 cm , where the mixing takes on a shear layer type of behavior, the BOAT ML predictions (Fig. 5.7a) are quite good in contrast to the predictions of the ML models in the other two codes. The BOAT kε2 predictions (Fig. 5.7b) are also quite good while those in the GENMIX code are somewhat poorer.

These comparisons show that both the ML and kε2 models in BOAT accurately predict a type of flow situation, which is quite analogous to the nearfield mixing layer downstream of nozzle boattails. In addition, they demonstrate that the performance of a turbulence model cannot be judged separately from the code in which it is contained. The noted differences in the model/code predictions are attributable to both minor variations in the specific model formulations within the codes as well as to variations in the computational aspects of the various codes such as grid distribution, shear layer growth expression, etc.

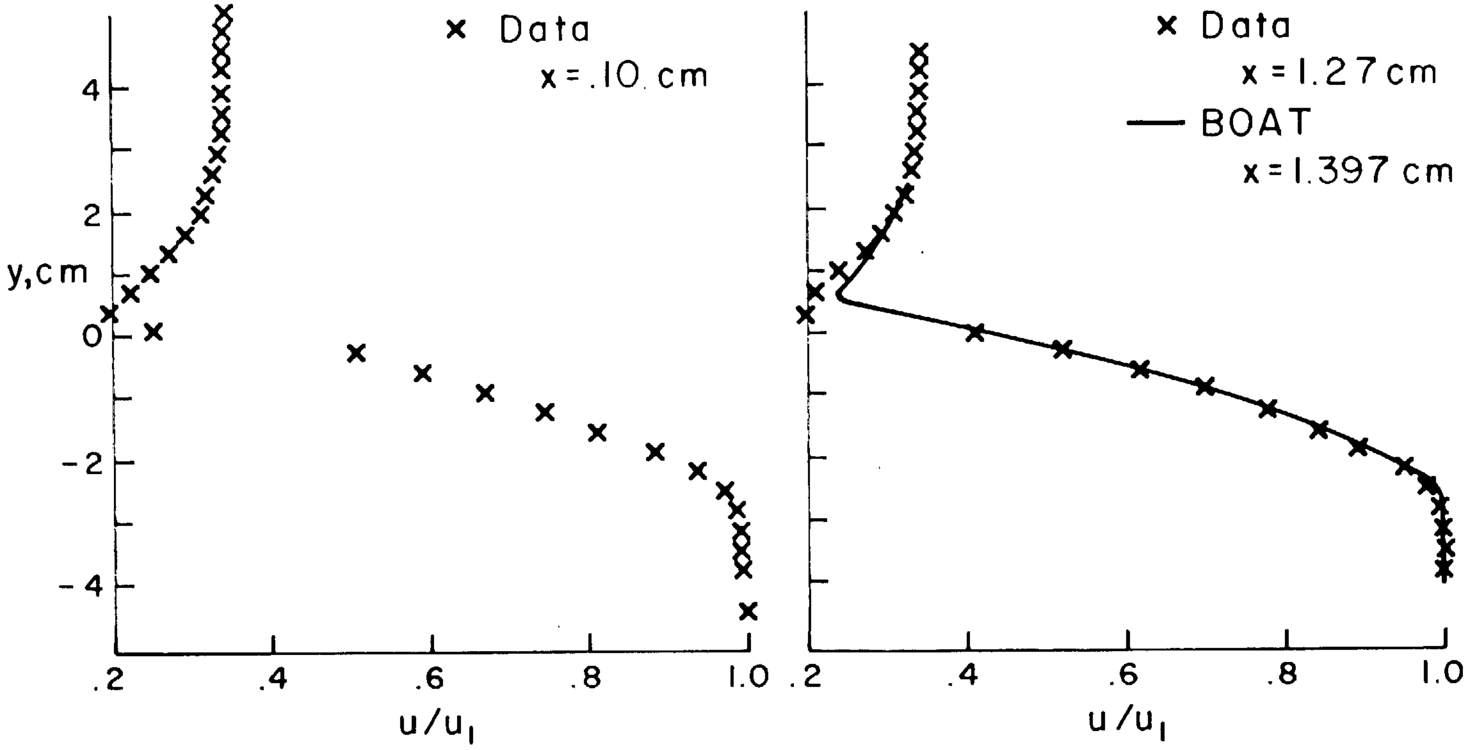

(a) (b)

Figure 5.4 Comparison of BOAT calculation with the experimental data of Lee for nonsimilar free shear layers — Prandtl mixing length model.

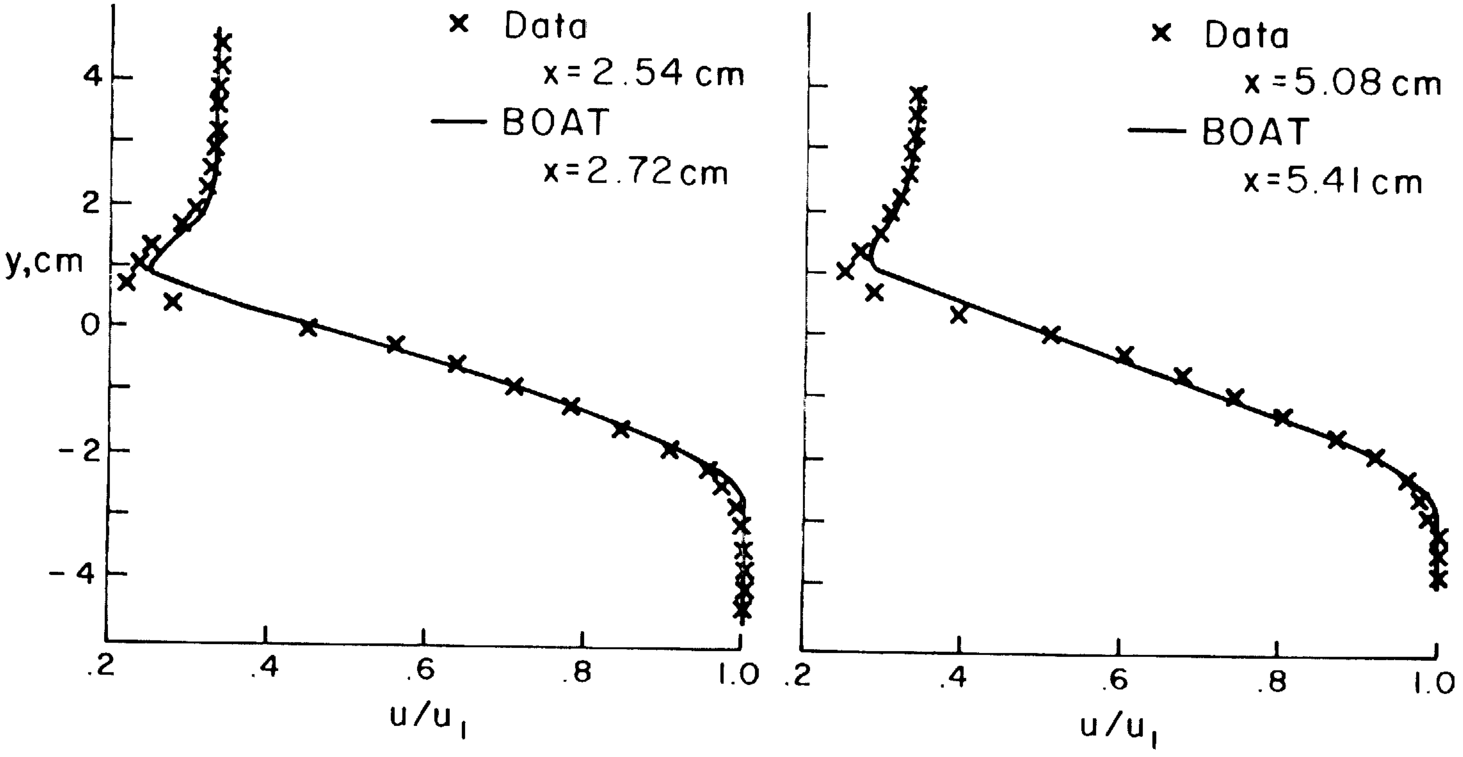

(c) (d)

Figure 5.4 (Continued) Comparison of BOAT calculation with the experimental data of Lee for nonsimilar free shear layers — Prandtl mixing length model.

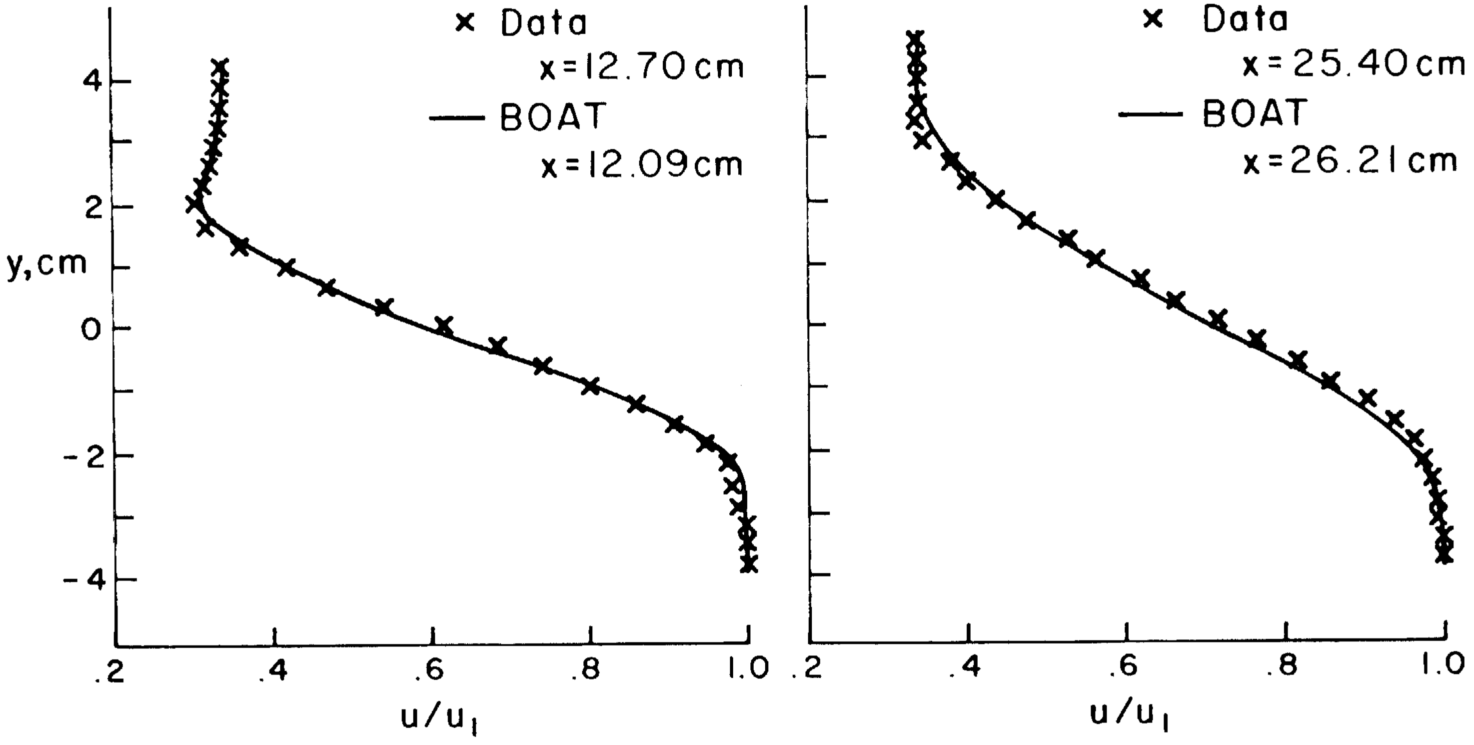

(e)

(f)

Figure 5.4 (Continued) Comparison of BOAT calculation with the experimental data of Lee for nonsimilar free shear layers — Prandtl mixing length model.

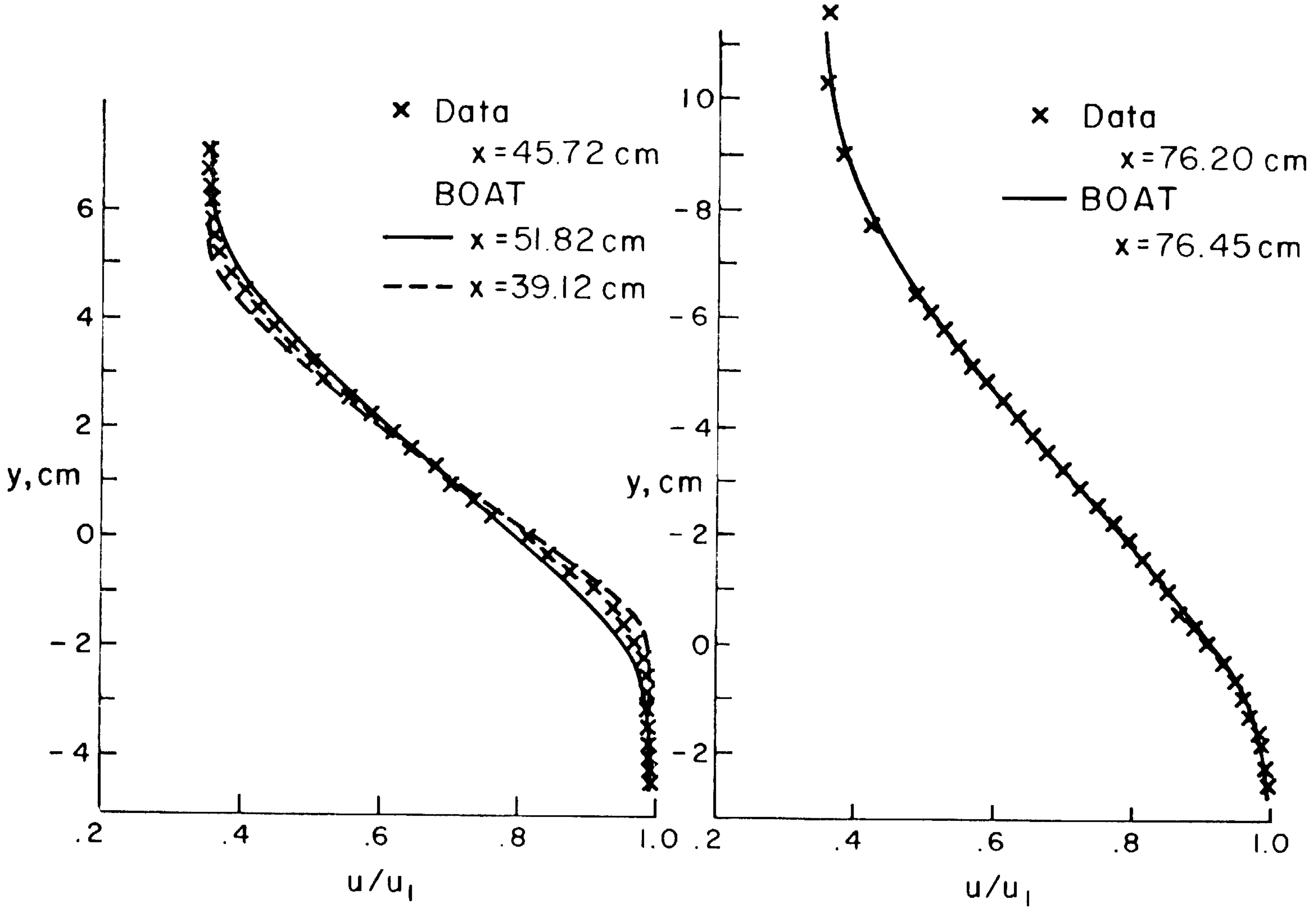

(g)

(h)

Figure 5.4 (Continued) Comparison of BOAT calculation with the experimental data of Lee for nonsimilar free shear layers — Prandtl mixing length model.

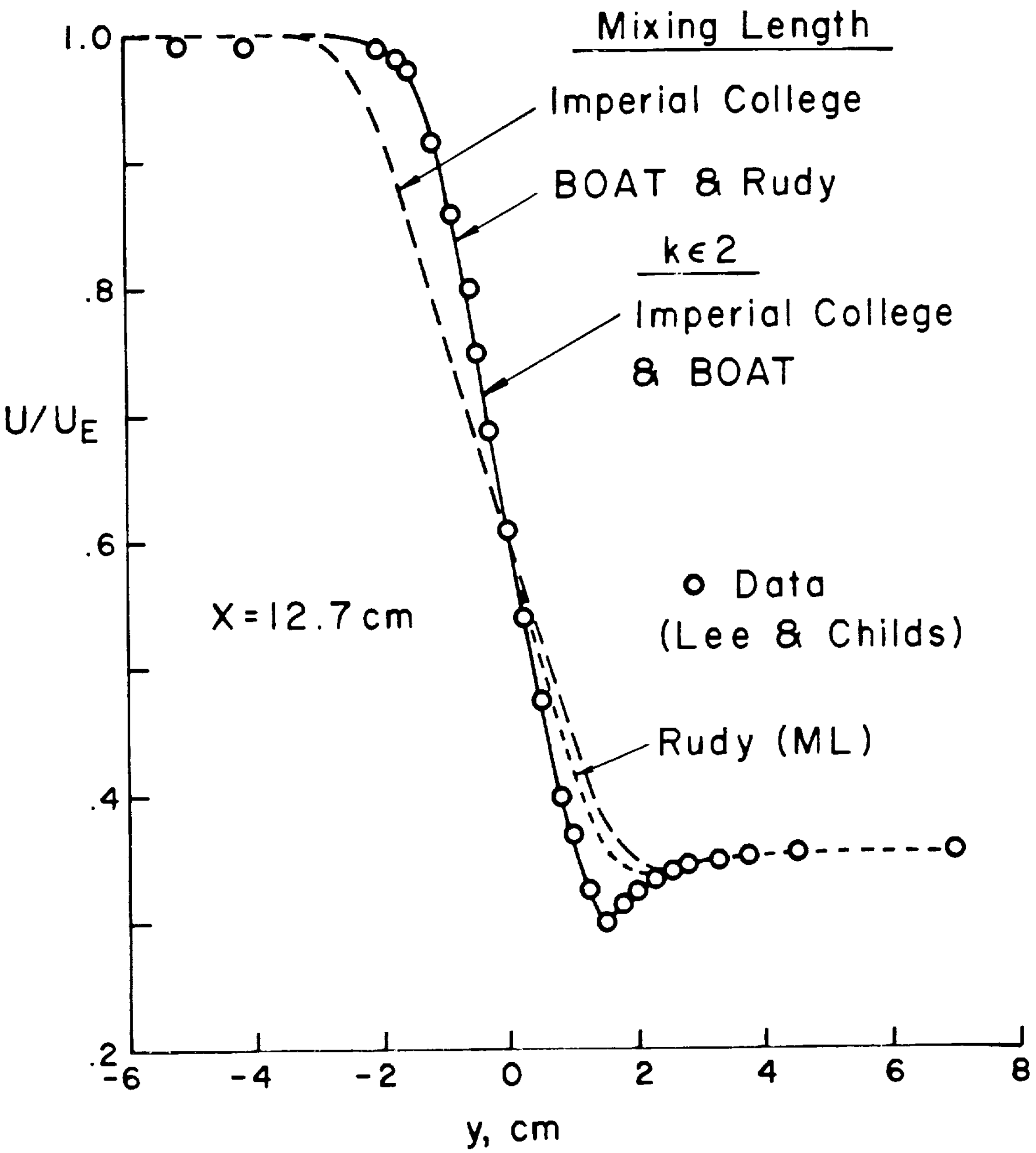

Figure 5.5 Comparison between predicted and measured velocity profiles for 2D shear layer with initial boundary layers.

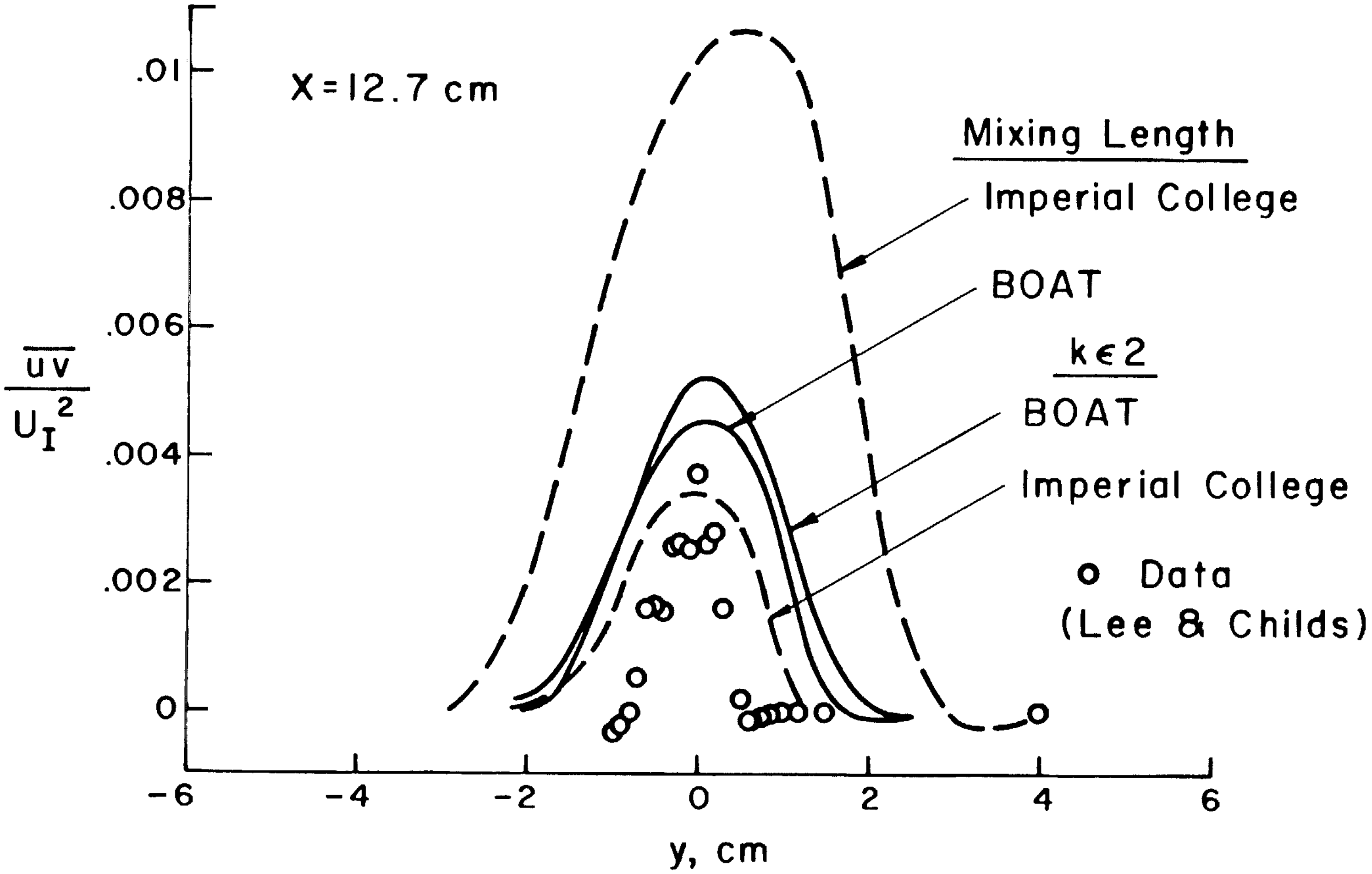

Figure 5.6 Comparison between predicted and measured shear stress profiles for 2D shear layer with initial boundary layers.

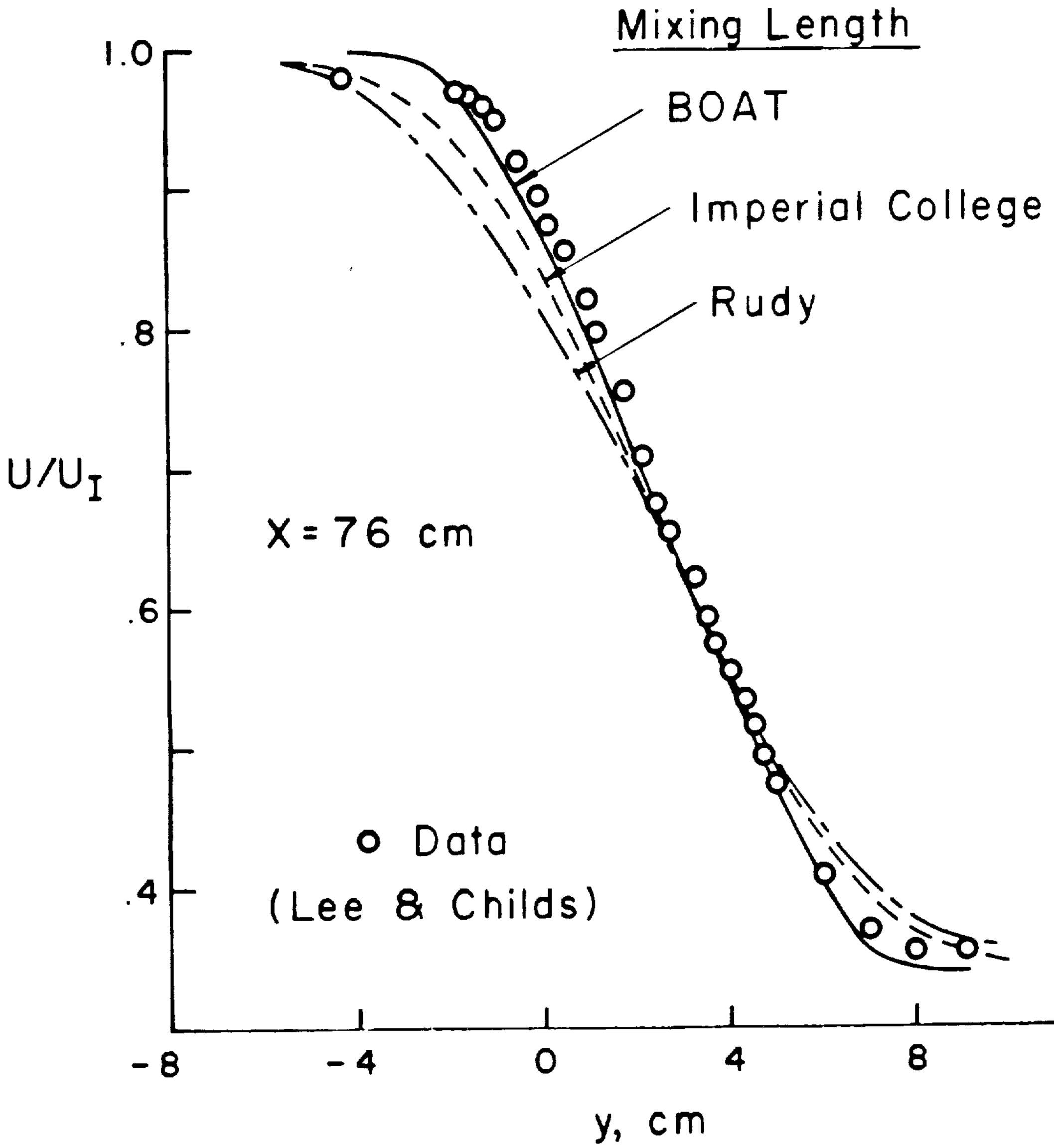

Figure 5.7a Comparison between predicted and measured velocity profiles for 2D shear layer with initial boundary layers.

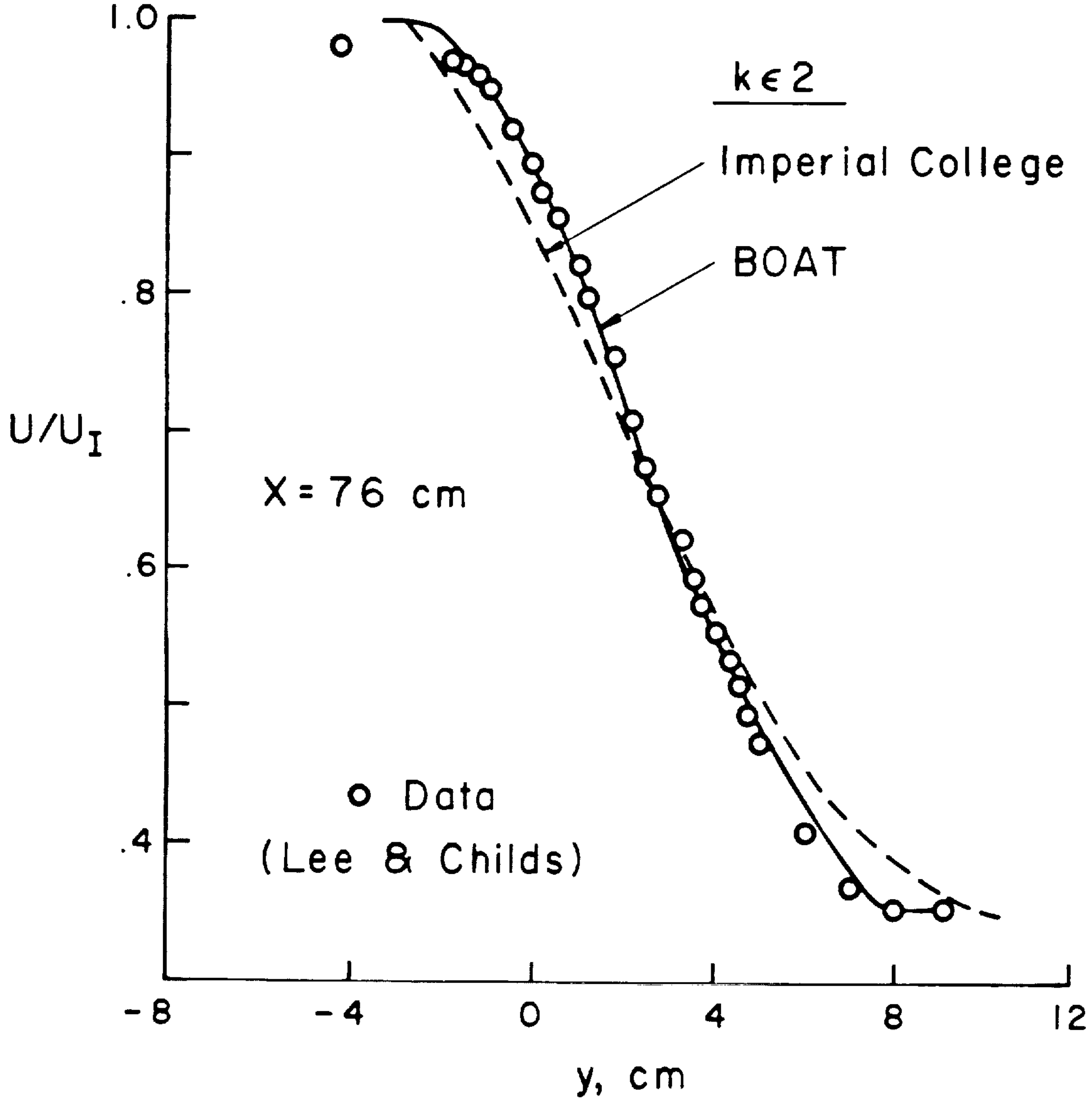

Figure 5.7b Comparison between predicted and measured velocity profiles for 2D shear layer with initial boundary layers.

Although the above comparisons are for incompressible flows, we expect that the BOAT code will be equally valid for the mildly compressible flow situations in typical aircraft exhausts (i.e., jet exhaust Mach numbers of approximately one, subsonic/transonic external streams). As demonstrated in the compilation of jet spreading rate data presented in Reference 13, noticeable reductions due to compressibility are associated with jet Mach numbers greater than 1.5 to 2 .

5.3 Coaxial Jet Mixing

Although nearfield mixing is of prime concern in this study, it is also of interest to demonstrate the validity of BOAT for farfield situations. This has been done via comparisons with coaxial jet mixing data. The value of $\ell/\delta = .08$ used for farfield axisymmetric situations in the ML model was, in fact, arrived at by matching farfield decay rates for jets into still air. In application of the ML model, the value of the ratio of ℓ/δ is changed from .065 to .08 abruptly when the mixing layer reaches the axis. It is expected that reasonable rates of mixing will be predicted for both the nearfield shear layer and in the farfield fully developed mixing layer. However, poorer agreement is anticipated in the transitional region where the turbulence processes are well out of equilibrium, and simple models predicated upon equilibrium assumptions may not be adequate. These statements are confirmed by the predictions achieved with the ML model in BOAT in analyzing the Forstall and Shapiro data[23] (Test Case 9 of the NASA Shear Flow Conference) for coaxial jet mixing. Figure 5.8 indicates that while the rate of velocity decay in the farfield is well predicted by the ML model, the performance in the transitional region ($5 < X/D_J < 30$) is poor and affects the overall quality of the results in the farfield. The kε2 model, however, does admirably in analyzing the nearfield, farfield, and transitional regions.

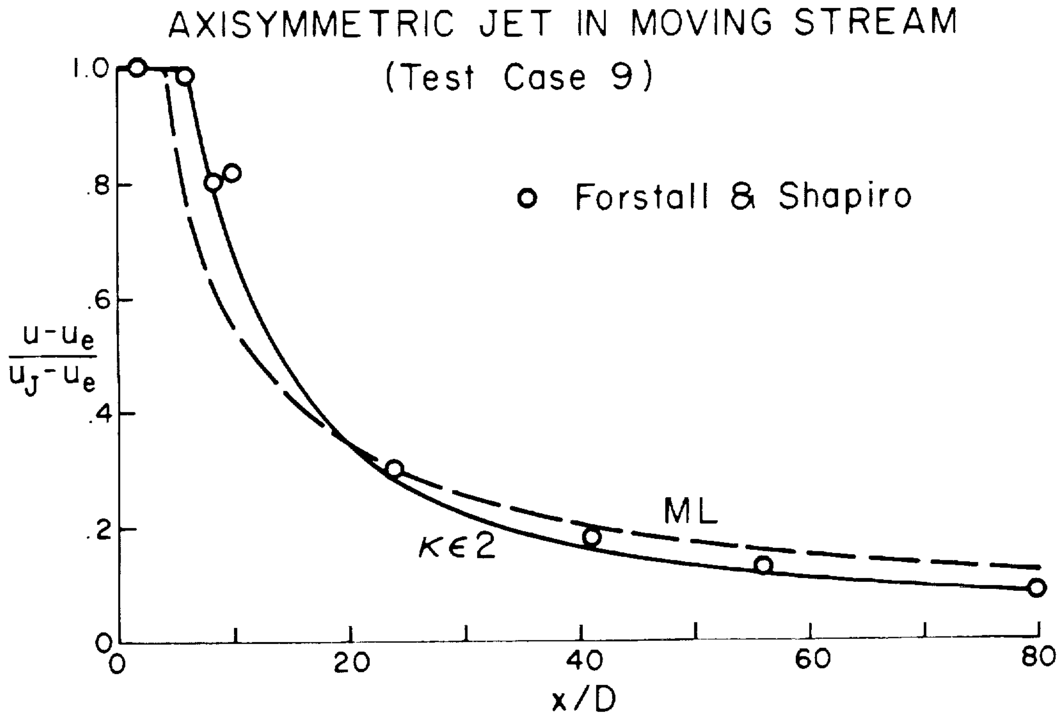

Figure 5.8 Comparison between centerline velocity decay predictions and data for an axisymmetric jet.

6. APPLICATIONS TO LABORATORY COLD AIR JETS

6.1 Displacement Thickness Type Correction to Inviscid Plume Geometry

For the cases to be considered below (which contain many of the essential features of actual aircraft exhaust flows), the external boundary layer thicknesses have been rather substantial (i.e., comparable in size to the nozzle exit radius as depicted in Figure 6.1). Thus, the streamline deflections associated with the entrainment process are primarily induced by the mixing away of the low velocity (wake-like) initial region. These deflections are comparable in magnitude to (or even larger than) those produced by purely inviscid processes. For analyzing the flow in such situations, the following procedure has been followed. In view of the rather small deflection angles along the plume interface, mixing processes along the interface are analyzed in standard cylindrical coordinates rather than in plume-oriented boundary layer coordinates. Then, the normal velocity, $v_e(x)$, at the outer shear layer edge is in the radial direction and includes contributions from both viscous (entrainment) and inviscid (blockage) processes. To account for the radial variation in v required to satisfy the continuity equation, the injection velocity, $v_j(x)$, to be applied along the interface for the subsequent external flowfield calculation, is obtained by modifying $v_e(x)$ via the relation

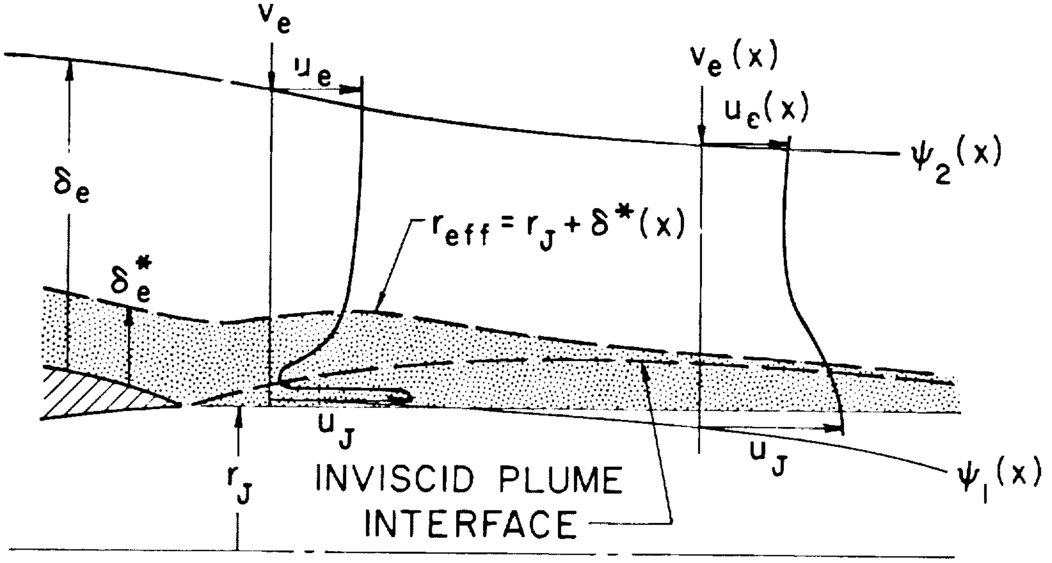

Figure 6.1 Determination of effective inviscid plume boundary shape for large initial boundary layers.

$$v_j(x) = \frac{\rho_e(x) r_e(x)}{\rho_j r_j} v_e(x) \tag{45}$$

Then, the "effective" plume boundary, $r_{eff}(x)$, is determined by adding $\delta^*(x)$ (obtained from $d\delta^*/dx = v_j/u_e$) to $r = r_j$, the $\delta^*(x)$ integration being initialized with the value of δ^* at the nozzle exit from the boundary layer calculation.

In terms of incorporating BOAT into the iterative patched LRC methodology, the following sequence of calculations is entailed:

(1) Iterative solution of exhaust/external flows without entrainment to yield inviscid flowfield maps and boundary layer properties at nozzle exit.

(2) Overlaid shear layer calculation employing inviscid flowfield maps to yield streamline deflections due to entrainment process.

(3) Plume geometry modification accounting for streamline deflections due to entrainment.

(4) External flow calculation repeated over afterbody and modified plume geometry.

(5) Exhaust flow calculation repeated employing pressure variation determined from external flow calculation.

Steps (2) through (5) can be repeated in a successive fashion until a converged viscous/inviscid flowfield solution is obtained. In this approach, the entrainment effect directly modifies the external flow structure and indirectly modifies the exhaust plume structure. The optimal procedure to be utilized in arriving at an overall converged solution has not been formalized. An assessment of alternative procedures is currently being investigated by R.G. Wilmoth at LRC. The cases reported below do not represent fully converged solutions but rather first-order entrainment corrected solutions employing steps (1) - (4) above.

6.2 Effective Cold Air Jet Boundaries

Preliminary results using BOAT within the patched LRC methodology have been obtained for one of the boattail nozzle configurations tested with cold air jets by Reubush[12]. Experimental boattail surface pressures are presented in Reference 12 for various free stream Mach numbers and jet total pressure ratios ($P_{t,j}/P_e$) . BOAT calculations were performed for a fully expanded ($P_{t,j}/P_e = 2$) and a modestly underexpanded jet ($P_{t,j}/P_e = 3$) with a nominal velocity ratio, u_2/u_1 , of about 0.5 , and free stream Mach number of 0.4 . Initial external boundary layers at the end of the boattail were quite thick in both cases.

The effective boundaries downstream of the nozzle exit for the two cases investigated are shown in Figure 6.2 ($x/r_j = 0$ corresponds to the end of the boattail, which is also the nozzle exit). Also shown are the inviscid plume interfaces obtained by the method of Reference 5 and the effective solid plume boundaries obtained by treating the inviscid plume interface as a solid body to which is added the calculated boundary layer displacemnt thickness. This latter boundary is commonly used to predict jet plume blockage effects without considering entrainment (e.g., see Reference 2). The important observation here is that when the effects of entrainment are considered, the effective plume boundary is substantially reduced in size primarily because the mass deficit, associated with the initial boundary layers, mixes away rather rapidly. Thus, treating the inviscid plume as a solid boundary is

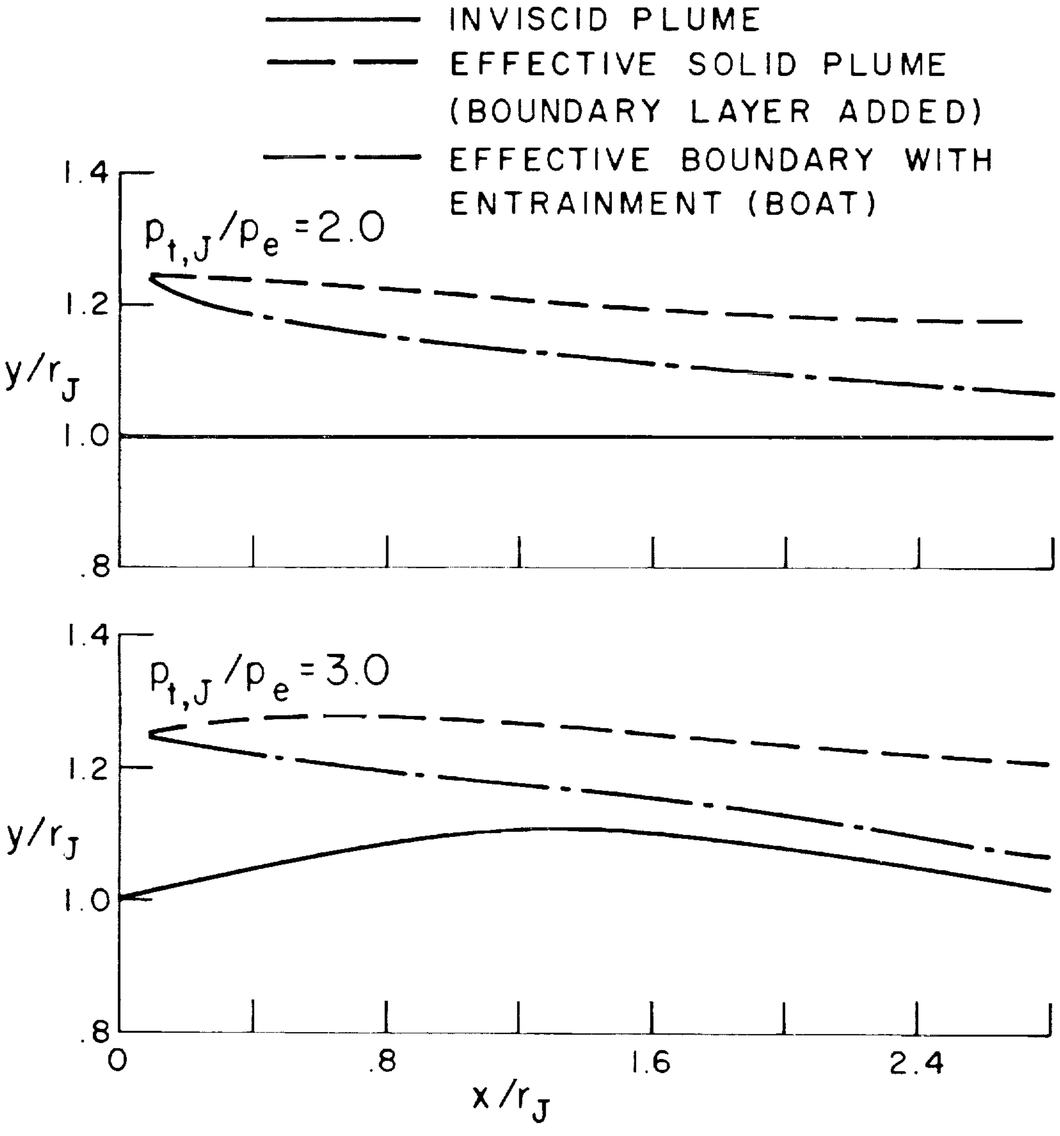

Figure 6.2 Comparison between effective boundary calculated by BOAT and effective solid plume for fully expanded and underexpanded jet mixing, $M_e = 0.40$, kε2 turbulence model.

quite unrealistic. Since jet aircraft nozzles are generally located in regions of thick boundary layers (e.g., near the aft end of the aircraft), a similar reduction in effective boundary size is expected.

6.3 Predicted and Measured Boattail Pressures

Boattail pressure distributions predicted by the inviscid code of Reference 4 using the effective solid plume (no entrainment) and the effective boundary (with entrainment) are compared with the experimental data in Figures 6.3a and b. A sketch of the boattail geometry and inviscid plume shape is also indicated. Excellent agreement with the experimental pressure distribution is obtained at both jet pressure ratios when entrainment effects are included, with a corresponding improvement in the predicted boattail drag coefficient, $C_{D,\beta}$. While the effect of underexpansion on the inviscid plume geometry appears relatively small (see Fig. 6.2), the pressure distribution is quite sensitive to this effect as evidenced by the variations in C_p downstream of the nozzle exit (Fig. 6.3). Including the (viscous) effect of entrainment decreases these variations, indicating a weakening of the effective wavelike amplitude of the inviscid plume. Such an effect is qualitatively similar to that produced by the boundary layer on the flow about a

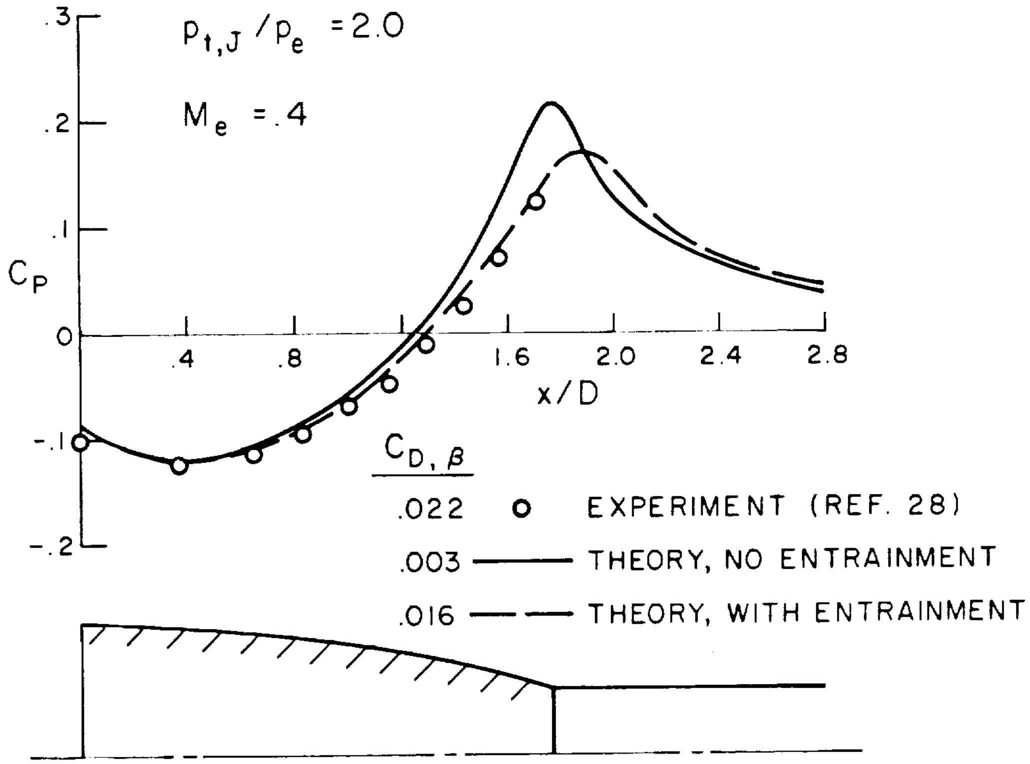

Figure 6.3a Effects of jet entrainment on boattail pressure distributions and comparison with experimental data, $M_e = 0.40$, kε2 turbulence model.

compression corner or expansion shoulder, i.e., a weakening of the "inviscid" wave structure. Based on these limited comparisons, the interactive entrainment model appears to provide a reasonable representation of the boattail flowfield.

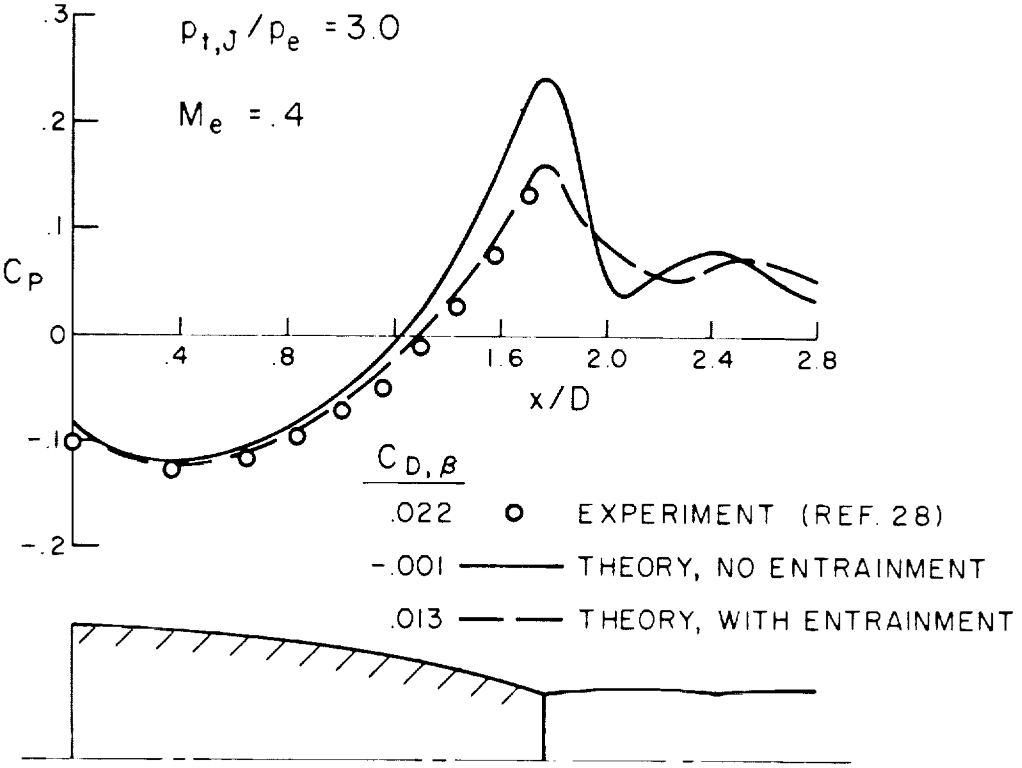

Figure 6.3b Effects of jet entrainment on boattail pressure distributions and comparison with experimental data, $M_e = 0.40$, $k\varepsilon 2$ turbulence model.

6.4 Sensitivity Studies

By varying some of the input and modeling parameters required for entrainment calculations, the relative dependence of the effective geometry (and hence boattail pressures) on these parameters can be established. Areas explored were initial boundary layer properties, turbulence models, and pressure gradients.

6.4.1 Sensitivity to initial boundary layer properties.- In the cases studied here (and for most cases of practical interest), the internal (nozzle) boundary layers are small with respect to the nozzle exit radius while the external (afterbody) boundary layers are relatively large. For the boattail configuration used for the calculations, nominal values of $\delta_1^*/r_j \sim .013$ (taken from Yaros[10]) and $\delta_2^*/r_j \sim .24$ were employed. Sensitivity studies in which the size (δ^*) and shape (u^*) parameters of the internal boundary layer were varied by a factor of 2 about their nominal values produced negligible changes in the effective plume geometry, as anticipated in view of the negligible internal boundary layer size. A similar variation of the shape factor for the external boundary layer (nominal value of $u_2^* \sim .033$), holding δ_2^* fixed, also produced negligible changes. Substantial variations in δ_2^* will, of course, have an appreciable effect on the effective plume geometry. However, since δ_2^* is supplied as part of the iterative external flow solution, it cannot be arbitrarily varied without further iterations between BOAT and the external flow code. This is quite time consuming with the present manual coupling between codes and not warranted in view of the rather obvious sensitivity of the effective geometry upon δ_2^* .

6.4.2 Sensitivity to turbulence models.- By performing the calculations with both a simple (ML) and more detailed (kε2) turbulence model, the level of sophistication required in the turbulence modeling can be assessed. Comparisons of the predicted effective boundary shape for both cases studied are given in Figure 6.4. In both cases, the ML model predicts a more rapid rate

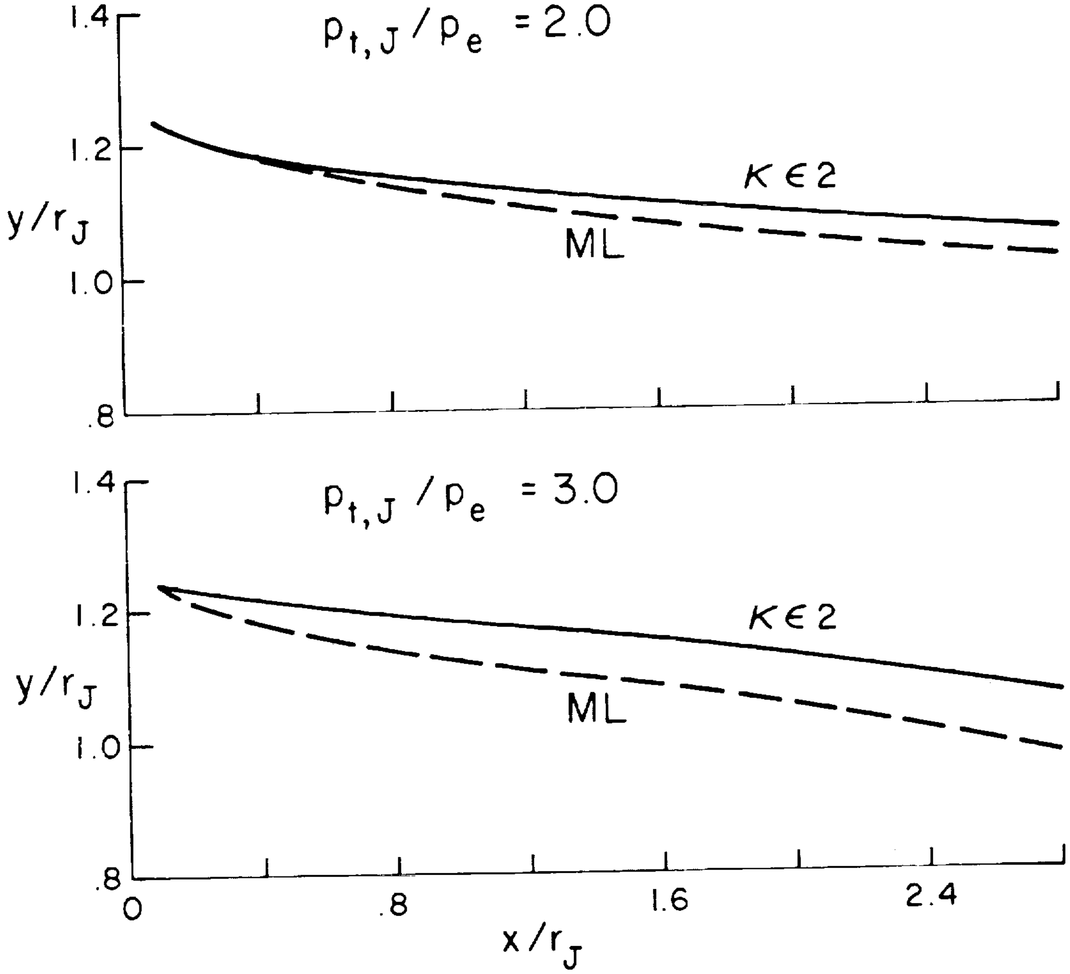

Figure 6.4 Effect of turbulence model on effective plume boundary shape.

of mixing (and corresponding rate of entrainment) than the kε2 model and thus a narrower effective plume geometry. The difference is substantially more pronounced in the underexpanded case where appreciable pressure gradients exist and the shear layer edge conditions are thus varying. Inviscid calculations over these geometries (and those for other similar test cases) have indicated that either the ML or kε2 model can yield a reasonable estimate of entrainment effects for fully expanded jets while the kε2 model produces more consistent results for underexpanded jets.

6.4.3 Sensitivity to pressure gradients.- To test the sensitivity of the present results to pressure gradients, BOAT calculations (with the kε2 model) were repeated with the pressure gradient terms in both the momentum and energy equations set identically to zero (while local values of density were computed employing the mapped inviscid pressures). A comparison of the effective plume geometry with and without pressure gradients is shown in Figure 6.5. With the pressure gradients deleted, the entrainment effect is markedly reduced; in fact, the effective boundary shapes are only slightly improved from those obtained treating the plume interface as a solid boundary (see Fig. 6.2 for comparison). Clearly, the favorable nearfield pressure gradients contribute strongly to accelerating the flow in the low velocity mass-deficit region and thus increase the overall entrainment rate. This marked effect of pressure gradients clearly rules out the isobaric assumptions used in previous entrainemnt models[10,11].

7. CONCLUDING REMARKS

1. The use of a "displacement thickness" (or normal injection velocity) correction to the inviscid plume boundary has been introduced to account for the effects of jet entrainment on the inviscid external subsonic/transonic flow calculation. A computational model (BOAT) has been developed which predicts the rate of jet entrainment via an overlaid, parabolic procedure from which the displacement thickness can be determined. Limited comparisons between predicted and measured boattail pressure distributions have been quite favorable, indicating that use of the BOAT code to calculate jet entrainment, in conjunction with the patched NASA/LRC system, shows great promise as a computational approach for predicting nozzle boattail drag.

2. The BOAT code has been shown to be a viable tool for calculating nearfield turbulent mixing processes. The application of both eddy viscosity (Prandtl mixing length) and two-equation (kε2) turbulence models within BOAT, enable it to adequately predict basic (constant pressure, nonreacting) free shear layers. Sensitivity studies have indicated that the kε2 model, which accounts for the turbulence "history," yields overall results of better quality for underexpanded, variable pressure plumes. The assessment of BOAT's capabilities at higher Mach numbers and for reacting/high temperature exhausts via comparisons with a broad based body of data (supersonic jets/shear layers, turbulent diffusion flames, rocket exhaust plume data, etc.) is in progress.

3. The boattail pressure changes produced by the entrainment correction to the inviscid plume boundary suggest that the weak viscous/inviscid

interaction approach adopted for this study may also be adequate for more generalized situations. The rather large influence of pressure gradients on the entrainment rate, in application of the overlaid methodology, clearly demonstrates the inadequacy of isobaric mixing assumptions employed in earlier modeling efforts. Further studies are in progress to assess the adequacy of the viscous-inviscid coupling procedure over a wider range of operating conditions.

4. An automated procedure for coupling the results of the various codes comprising the patched viscous/inviscid model is in progress at LRC. Toward this end, a new inviscid exhaust plume code has been developed which will be directly coupled with the BOAT code providing a one-pass solution of the plume and mixing layer. The inviscid code employs shock-capturing methodology[24,25] in a mapped coordinate grid and has been tailored for ease of operation and extremely fast run time.

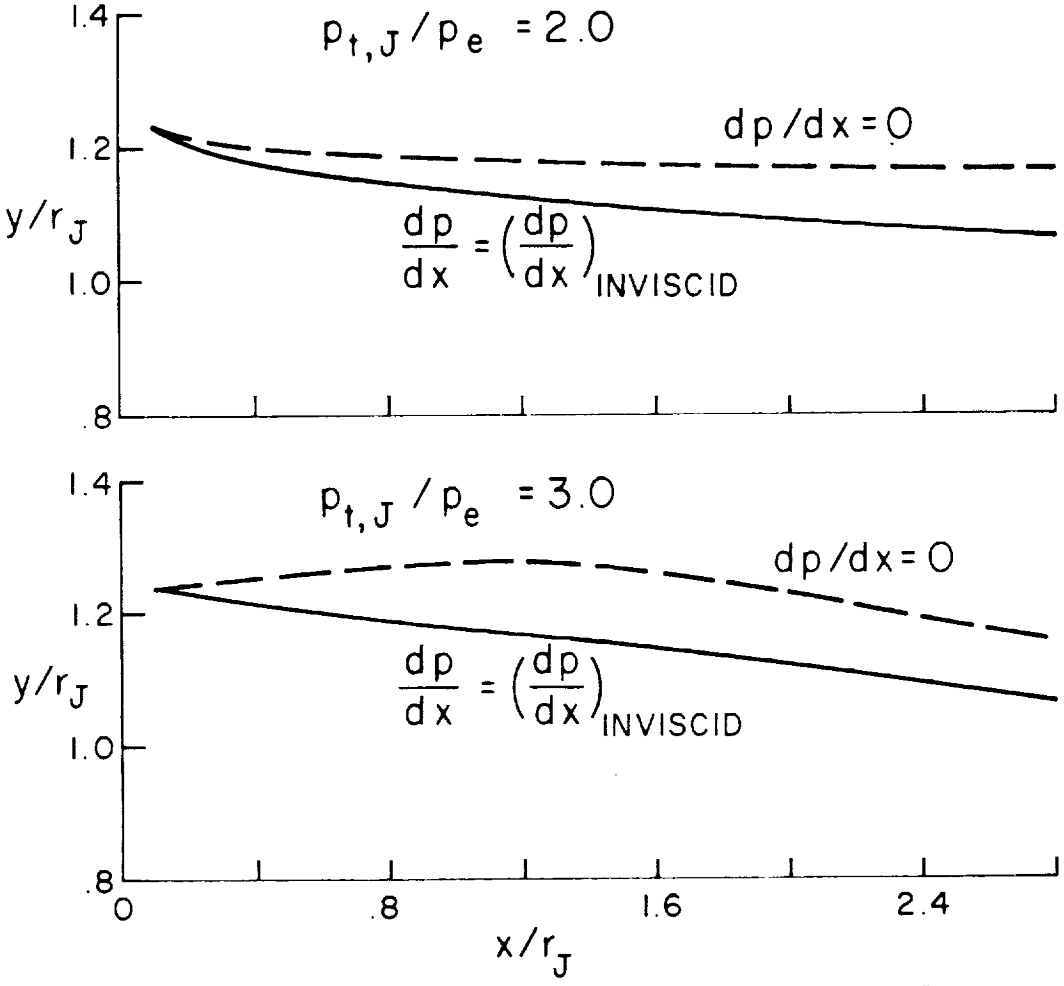

Figure 6.5 Effect of pressure gradient on effective plume boundary shape, kε2 turbulence model.

5. An evaluation of turbulence models for application to afterburning rocket and aircraft plumes is in progress (under NWC support) using the BOAT code. Specific objectives and preliminary findings are reported in Reference 26. The study should yield valuable information regarding the choice of turbulence models in extending BOAT to situations with combustion and marked compressibility.

REFERENCES

1. Reubush, D.E.; and Putnam, L.E.: An Experimental and Analytical Investigation of the Effect on Isolated Boattail Drag of Varying Reynolds Number Up to 130 x 10^6. NASA TN D-8210, May 1976.

2. Putnam, L.E.; and Abeyounis, W.K.: Experimental and Theoretical Study of Flow Fields Surrounding Boattail Nozzles at Subsonic Speeds, AIAA Paper No. 76-765, July 1976.

3. Wilmoth, R.G.: Analytical Study of Viscous Effects on Transonic Flow over Boattail Nozzles. AIAA Paper No. 77-223, January 1977.

4. South, J.D., Jr.; and Jameson, A.: Relaxation Solutions for Inviscid Axisymmetric Transonic Flow over Blunt or Pointed Bodies. Proceedings of the AIAA Computational Fluid Dynamics Conference, July 1973, pp. 8-17.

5. Salas, M.D.: The Numerical Calculation of Inviscid Plume Flow Fields. AIAA Paper No. 74-523, June 1974.

6. Reshotko, E.; and Tucker, M.: Approximate Calculation of the Compressible Turbulent Boundary Layer with Heat Transfer and Arbitrary Pressure Gradient. NASA TN 4154, 1957.

7. Mikatarian, R.R.; Kau, C.J.; and Pergament, H.S.: A Fast Computer Program for Nonequilibrium Rocket Plume Predictions. AFRPL-TR-72-94, August 1972.

8. Patankar, S.W.; and Spalding, D.B.: Heat and Mass Transfer in Boundary Layers. Second ed. Intertext Books (London), 1970.

9. Dash, S.; Boccio, J.; and Weilerstein, G.: A Computational System for the Prediction of Low Altitude Rocket Plume Flowfields: Volume I - Integrated System; Volume II - Inviscid Plume Model (MAXIPLUM); Volume III - Mixing/Afterburning Model (CHEMX): GASL TR-239, General Applied Science Laboratories, Inc., Westbury, NY, December 1976.

10. Yaros, S.F.: An Analysis of Transonic Viscous/Inviscid Interactions on Axisymmetric Bodies with Solid Stings or Real Plumes. Ph.D. Dissertation, Univ. of Tennessee, 1977.

11. Grossman, B.; and Melnik, R.: The Numerical Computation of the Transonic Flow Over Afterbodies Including the Effect of Jet-Plume and Viscous Interactions. AIAA Paper No. 75-62, January 1975.

12. Reubush, D.E.: Experimental Study of the Effectiveness of Cylindrical Plume Simulators for Predicting Jet-On Boattail Drag at Mach Numbers up to 1.30. NASA TN D-7795, 1974.

13. Free Turbulent Shear Flows, Volume I - Conference Proceedings. NASA SP-321, July 1972.

14. Dash, S.M.; and Pergament, H.S.: The Analysis of Low Altitude Rocket and Aircraft Plume Flowfields: Modeling Requirements and Procedures. Proceedings of the JANNAF 10th Plume Technology Meeting, CPIA Pub. 291, Vol I, 1977, pp. 53-132.

15. Launder, B.E.; et al.: Prediction of Free Shear Flows: A Comparison of Six Turbulence Models. Free Turbulent Shear Flows, Vol. I - Conference Proceedings. NASA SP-321, July 1972, pp. 361-426.

16. Pope, S.B.: An Explanation of the Turbulent Round-Jet/Plane-Jet Anomaly. AIAA J., Vol 16, March 1978, pp. 279-281.

17. Chien, J.C.: Numerical Computation of Subsonic Conical Diffuser Flows with Nonuniform Turbulent Inlet Conditions. AEDC TR-77-78, September 1977.

18. Abramovich, G.N.: The Theory of Turbulent Jets. M.I.T. Press (Cambridge, MA), 1963.

19. Hinze, J.O.: Turbulence. Second ed. McGraw-Hill, 1975.

20. Rodi, W.: A Review of Experimental Data of Uniform Density Free Turbulent Boundary Layers. Launder, B.E., ed.: Studies in Convection, Vol. I. Academic Press (London), 1975, pp. 79-166.

21. Lee, S.L.: A Study of the Two-Dimensional Free Turbulent Mixing Between Converging Streams With Initial Boundary Layers. Ph.D. Dissertation, Univ. of Washington, 1966.

22. Rudy, D.H.; and Bushnell, D.M.: A Rational Approach to the Use of Prandtl's Mixing Length Model in Free Turbulent Shear Flow Calculations. Free Turbulent Shear Flows, Vol. I - Conference Proceedings. NASA SP-321, July 1972, pp. 67-138.

23. Forstall, W., Jr.; and Shapiro, A.H.: Momentum and Mass Transfer in Coaxial Gas Jets. J. Appl. Mech., Vol. 17, No. 4, December 1950, pp. 399-408.

24. Dash, S.M.; and DelGuidice, P.D.: Analysis of Three-Dimensional Ducted and Exhaust Plume Flowfields. AIAA J., Vol. 16, August 1978, pp. 823-830.

25. Dash, S.M.; and DelGuidice, P.D.: Shock Capturing Finite-Difference and Characteristic Reference Plane Techniques for the Prediction of Three-Dimensional Nozzle-Exhaust Flowfields. NASA CR 145366, May 1978.

26. Pergament, H.S.; Dash, S.M.; and Fishburne, E.S.: Methodology for the Evaluation of Turbulence Models for Afterburning Rocket and Aircraft Plumes. Proceedings of the JANNAF 10th Plume Technology Meeting, CPIA Pub. 291, Vol. I, 1977, pp. 133-172.

1. Report No. NASA CR-3075	2. Government Accession No.	3. Recipient's Catalog No.

4. Title and Subtitle
A Computational Model for the Prediction of Jet Entrainment in the Vicinity of Nozzle Boattails (The BOAT Code)

5. Report Date
December 1978

6. Performing Organization Code

7. Author(s)
Sanford M. Dash and Harold S. Pergament

8. Performing Organization Report No.

10. Work Unit No.

9. Performing Organization Name and Address
Aeronautical Research Associates of Princeton, Inc.
50 Washington Road
Princeton, NJ 08540

11. Contract or Grant No.
NAS1-14794

13. Type of Report and Period Covered
Contractor Report

12. Sponsoring Agency Name and Address
National Aeronautics and Space Administration
Washington, D.C. 20546

14. Sponsoring Agency Code
505-04-13-01

15. Supplementary Notes
NASA Project Manager: Richard G. Wilmoth, NASA - Langley Research Center
Topical Report

16. Abstract

The development of a computational model (BOAT) for calculating nearfield jet entrainment, and its incorporation in an existing methodology for the prediction of nozzle boattail pressures, is discussed. BOAT accounts for the detailed turbulence and thermochemical processes occurring in the mixing layer formed between a jet exhaust and and surrounding external stream while interfacing with the inviscid exhaust and external flowfield regions in an overlaid, interactive manner. The ability of the BOAT model to analyze simple free shear flows is assessed by detailed comparisons with fundamental laboratory data. The overlaid procedure for incorporating variable pressures into BOAT and the entrainment correction employed to yield an "effective" plume boundary for the inviscid external flow are demonstrated. This is accomplished via application of BOAT in conjunction with the codes comprising the NASA/LRC patched viscous/inviscid methodology for determining nozzle boattail drag for subsonic/transonic external flows. An assessment of the overall approach is provided via comparisons between these predictions and data for underexpanded laboratory cold air jets. A manual describing the operation of the BOAT code comprises a supplement to this report.

17. Key Words (Suggested by Author(s)) Jet Entrainment Free Shear Layers Turbulence Models Displacement Thickness Viscous/Inviscid Interactions	18. Distribution Statement Unclassified - Unlimited Subject Category 34

19. Security Classif. (of this report) Unclassified	20. Security Classif. (of this page) Unclassified	21. No. of Pages 58	22. Price* $5.25

*For sale by the National Technical Information Service, Springfield, Virginia 22161

NASA-Langley, 1978